iScience

CellPress
OPEN ACCESS

Article

Skeletal-Muscle Metabolic Reprogramming in ALS-SOD1^{G93A} Mice Predates Disease Onset and Is A Promising Therapeutic Target

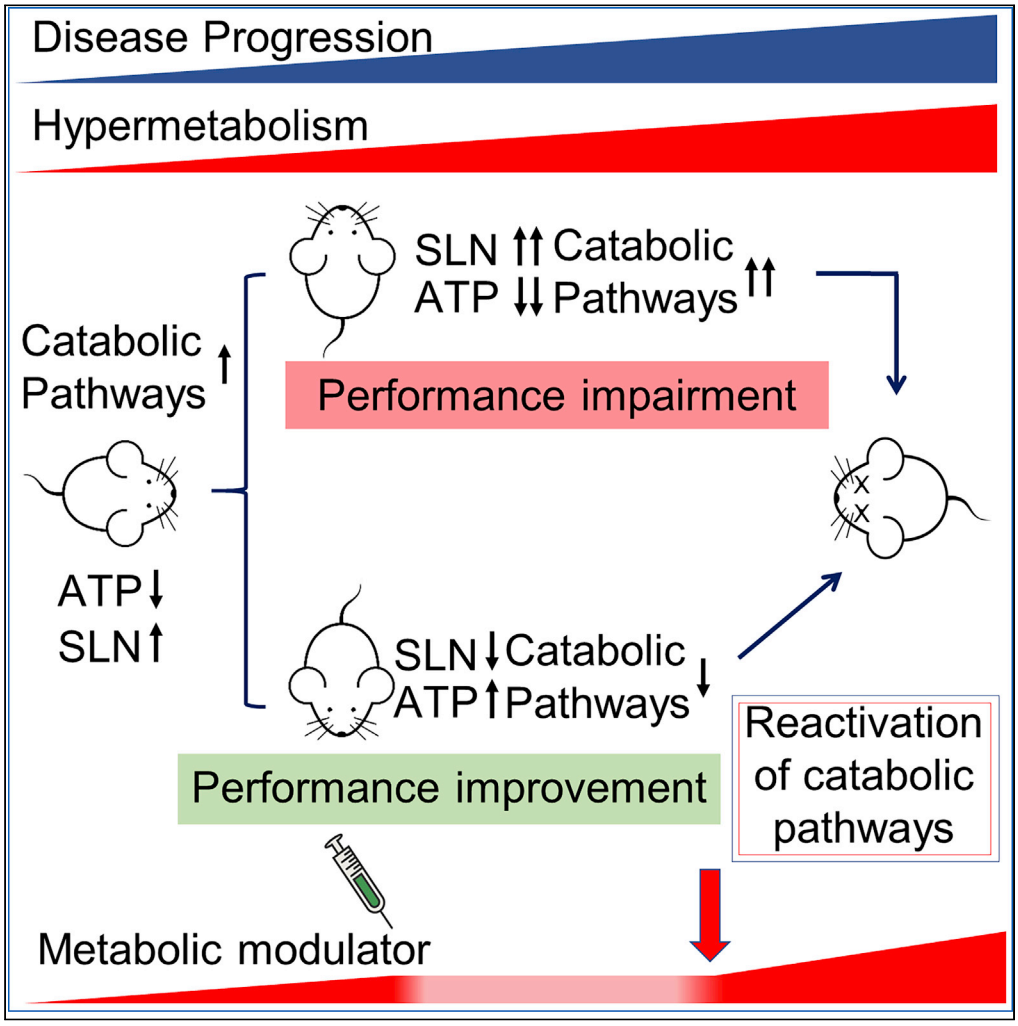

Silvia Scaricamazza, Illari Salvatori, Giacomo Giacovazzo, ..., Roberto Coccurello, Cristiana Valle, Alberto Ferri

c.valle@hsantalucia.it (C.V.)
alberto.ferri@cnr.it (A.F.)

HIGHLIGHTS

Metabolic switch use occurs early in the skeletal muscle of SOD1^{G93A} mice

Mitochondrial impairment precedes locomotor deficits and evokes catabolic pathways

Sarcolipin upregulation in presymptomatic SOD1^{G93A} mice precedes hypermetabolism

Pharmacological modulation of hypermetabolism improves locomotor performance

Scaricamazza et al., iScience *23*, 101087
May 22, 2020
https://doi.org/10.1016/j.isci.2020.101087

iScience

CellPress
OPEN ACCESS

Article

Skeletal-Muscle Metabolic Reprogramming in ALS-SOD1^{G93A} Mice Predates Disease Onset and Is A Promising Therapeutic Target

Silvia Scaricamazza,[1,2,14] Illari Salvatori,[2,14] Giacomo Giacovazzo,[2] Jean Philippe Loeffler,[3,4] Frederique Renè,[3,4] Marco Rosina,[1] Cyril Quessada,[3,4] Daisy Proietti,[2] Constantin Heil,[2] Simona Rossi,[1,5] Stefania Battistini,[6] Fabio Giannini,[6] Nila Volpi,[6] Frederik J. Steyn,[7,8] Shyuan T. Ngo,[8,9,10] Elisabetta Ferraro,[11] Luca Madaro,[2,12] Roberto Coccurello,[2,13] Cristiana Valle,[2,5,*] and Alberto Ferri[2,5,15,*]

SUMMARY

Patients with ALS show, in addition to the loss of motor neurons in the spinal cord, brainstem, and cerebral cortex, an abnormal depletion of energy stores alongside hypermetabolism. In this study, we show that bioenergetic defects and muscle remodeling occur in skeletal muscle of the SOD1^{G93A} mouse model of ALS mice prior to disease onset and before the activation of muscle denervation markers, respectively. These changes in muscle physiology were followed by an increase in energy expenditure unrelated to physical activity. Finally, chronic treatment of SOD1^{G93A} mice with Ranolazine, an FDA-approved inhibitor of fatty acid β-oxidation, led to a decrease in energy expenditure in symptomatic SOD1^{G93A} mice, and this occurred in parallel with a robust, albeit temporary, recovery of the pathological phenotype.

INTRODUCTION

Amyotrophic lateral sclerosis (ALS) is characterized by the progressive loss of upper and lower motor neurons. The loss of these neurons leads to the concomitant development of skeletal muscle atrophy (Rossi et al., 2015). ALS is a disease of obscure etiology, for which neither a cure nor a therapeutic option is available. ALS is a multifactorial disease and a number of mechanisms have been proposed to underpin disease pathology, including alterations in RNA metabolism, oxidative stress, axonal transport defects, neuroinflammation, impaired protein homeostasis, alterations in autophagic flux, aberrant cytoplasmic-nuclear shuttling, failure in DNA repair, excitotoxicity, mitochondrial dysfunction, and vesicular transport defects (Mejzini et al., 2019).

In spite of its elusive etiology, some well-described clinical signs in patients with ALS highlight promising lines of investigation to improve our understanding of disease. Notably, hypermetabolism (Steyn et al., 2018) and weight loss (Moglia et al., 2019) are associated with worse prognosis. However, weight loss, undernutrition, muscle atrophy, weakness, and reduced physical activity (Ioannides et al., 2016) appear incompatible with clinical studies reporting increased energy expenditure (EE) in patients with ALS (Bouteloup et al., 2009; Desport et al., 2005; Funalot et al., 2009; Kasarskis et al., 2014). The paradox may be reconciled by assuming that skeletal muscle plays a pathological role in ALS, contributing to defective energy metabolism and a derangement of basal metabolic rate. Indeed, skeletal muscle is a key determinant of whole-body metabolic rate (Zurlo et al., 1990).

In this context, the early events underlying defective muscle metabolism in ALS as well as the major molecular mechanisms that cause ALS-associated hypermetabolism are still unknown. We therefore undertook this investigation to provide insights into the early pathological events involved in ALS by examining the mechanisms responsible for maladaptive muscle oxidative metabolism and disease progression. Finally, in this study, we provided evidences to show that pharmacological modulation of metabolism can curtail excessive EE and improve ALS pathology, thereby demonstrating that limiting hypermetabolism could be a promising therapeutic target in ALS.

[1]University of Rome Tor Vergata, Department of Biology, Rome, Italy

[2]IRCCS Fondazione Santa Lucia, Rome, Italy

[3]Université de Strasbourg, UMR_S 1118, Strasbourg, France

[4]INSERM, U1118, Central and Peripheral Mechanisms of Neurodegeneration, Strasbourg, France

[5]National Research Council, Institute of Translational Pharmacology (IFT), Rome, Italy

[6]University of Siena, Department of Medical, Surgical and Neurological Science, Siena, Italy

[7]School of Biomedical Sciences, The University of Queensland, Brisbane, QLD, Australia

[8]Centre for Clinical Research, The University of Queensland, Brisbane, QLD, Australia

[9]Australian Institute for Bioengineering and Nanotechnology, The University of Queensland, Brisbane, QLD, Australia

[10]Queensland Brain Institute, The University of Queensland, Brisbane, QLD, Australia

[11]Department of Biology, University of Pisa, Pisa, Italy

[12]DAHFMO-Unit of Histology and Medical Embryology, Sapienza University of Rome, Rome, Italy

[13]National Research Council, Institute for Complex System (ISC), Rome, Italy

[14]These authors contributed equally

[15]Lead Contact

*Correspondence: c.valle@hsantalucia.it (C.V.), alberto.ferri@cnr.it (A.F.)

https://doi.org/10.1016/j.isci.2020.101087

RESULTS

An Increase in Fatty Acid Oxidation and Glucose Intolerance Precedes Hypermetabolism in SOD1^{G93A} Mice

To investigate the whole-body metabolic status and fuel oxidation in SOD1^{G93A} mice, we conducted indirect calorimetry over 2 or 3 continuous days. Measures were obtained from animals at the early presymptomatic (55 days of age) and symptomatic (120 days of age) stages of disease. Hypermetabolism, defined as an increase in total EE or resting energy expenditure (REE), was not detectable in early presymptomatic mice (Figures 1A–1C) but was strongly evident in symptomatic mice (Figures 1D–1F). Analysis of the respiratory exchange ratio (RER) revealed a significant genotype effect, with RER being reduced in both early presymptomatic and symptomatic SOD1^{G93A} mice when compared with wild-type control mice (Figures 1G and 1H). These results are indicative of enhanced fatty acid oxidation and predominant use of fatty acids as fuel source in ALS mice.

After confirmed metabolic alteration in presymptomatic SOD1^{G93A} mice and since skeletal muscle is the major factor affecting EE also at rest (Zurlo et al., 1990) we carried out RNA sequencing to assay gene expression changes in the *tibialis anterior* (TA) of SOD1^{G93A} mice at the onset stage of disease, when compared with their wild-type littermate controls. Gene enrichment analysis, using Reactome categories, highlighted that the gene sets most significantly enriched among downregulated genes were associated with glucose metabolism (Figure 1I). In particular, we observed downregulation of key glycolysis pathway genes (Figures 1J and 1K). The decrease in the expression of glycolytic pathway genes was further supported through our assessment of glucose tolerance in SOD1^{G93A} mice. At the early presymptomatic stage, SOD1^{G93A} mice already show a marked decrease in blood glucose clearance with respect to wild-type control littermates (Figure 1L, upper panel). This metabolic alteration dramatically worsened with disease progression in SOD1^{G93A} mice (Figure 1L, middle and lower panels).

ALS Skeletal Muscles Undergo Metabolic Reprogramming

Based on results obtained through indirect calorimetry and transcriptome analysis, we aimed to define the timing of the onset of metabolic changes in skeletal muscle of SOD1^{G93A} mice by analyzing the oxidative capacity of the glycolytic TA at different time points. We found that *in situ* NADH-TR and SDH activities were dramatically increased in SOD1^{G93A} mice at the early presymptomatic stage (55 days) and to a higher degree at the later stages of the disease (Figures 2A, 2B, S1A, and S1B).

In line with the rise in muscle oxidative capacity, we detected, by immunofluorescence analysis, a consistent increase in the intensity of ATPB, a known mitochondrial marker, in the TA muscle of SOD1^{G93A} mice (Figures 2C and S1C). Accordingly, a striking increase in mitochondrial mass was observed, defined by an increase in the amount (μg) of mitochondria per milligram of tissue as well as an increase in the content of mitochondrial DNA, in different muscles of SOD1^{G93A} mice during the course of the disease (Figures S2A–S2C). Interestingly, this phenomenon occurred mainly in glycolytic muscles and not in the oxidative *soleus* muscle.

The switching of skeletal muscle metabolism toward an oxidative phenotype in SOD1^{G93A} mice was further corroborated by the upregulation in neuron-derived orphan nuclear receptor (Nor1) mRNA in the TA (Figure 2D). This transcription factor is known to promote muscle remodeling toward oxidative metabolism by activating pathways critical for adaptation to exercise or energy deficit (Goode et al., 2016). The upregulation of Nor1 in SOD1^{G93A} mice occurred alongside an upregulation in mRNA encoding for myoglobin (Figure 2D) (Pearen et al., 2013). Moreover, we found significant alterations in the expression of mRNAs encoding myosin heavy chain isoforms. Specifically, we observed a reduction in the expression of the glycolytic isoform MyCHIIb and an increase in the expression of the oxidative/intermediate isoforms MyHCIIa and MyHCIIx (Figure 2E). No significant alterations were observed in the expression of the oxidative isoform MyHCI (Figure 2E). Overall, these data show that, in SOD1^{G93A} mice, glycolytic muscles undergo a profound rearrangement in their physiology throughout the course of disease.

Mitochondrial Bioenergetics Are Perturbed in Skeletal Muscle of Early Presymptomatic SOD1^{G93A} Mice

The metabolic modifications of skeletal muscle observed in SOD1^{G93A} animals mirror adaptations to endurance training, wherein a switch from glycolytic to oxidative metabolism occurs (Granata et al.,

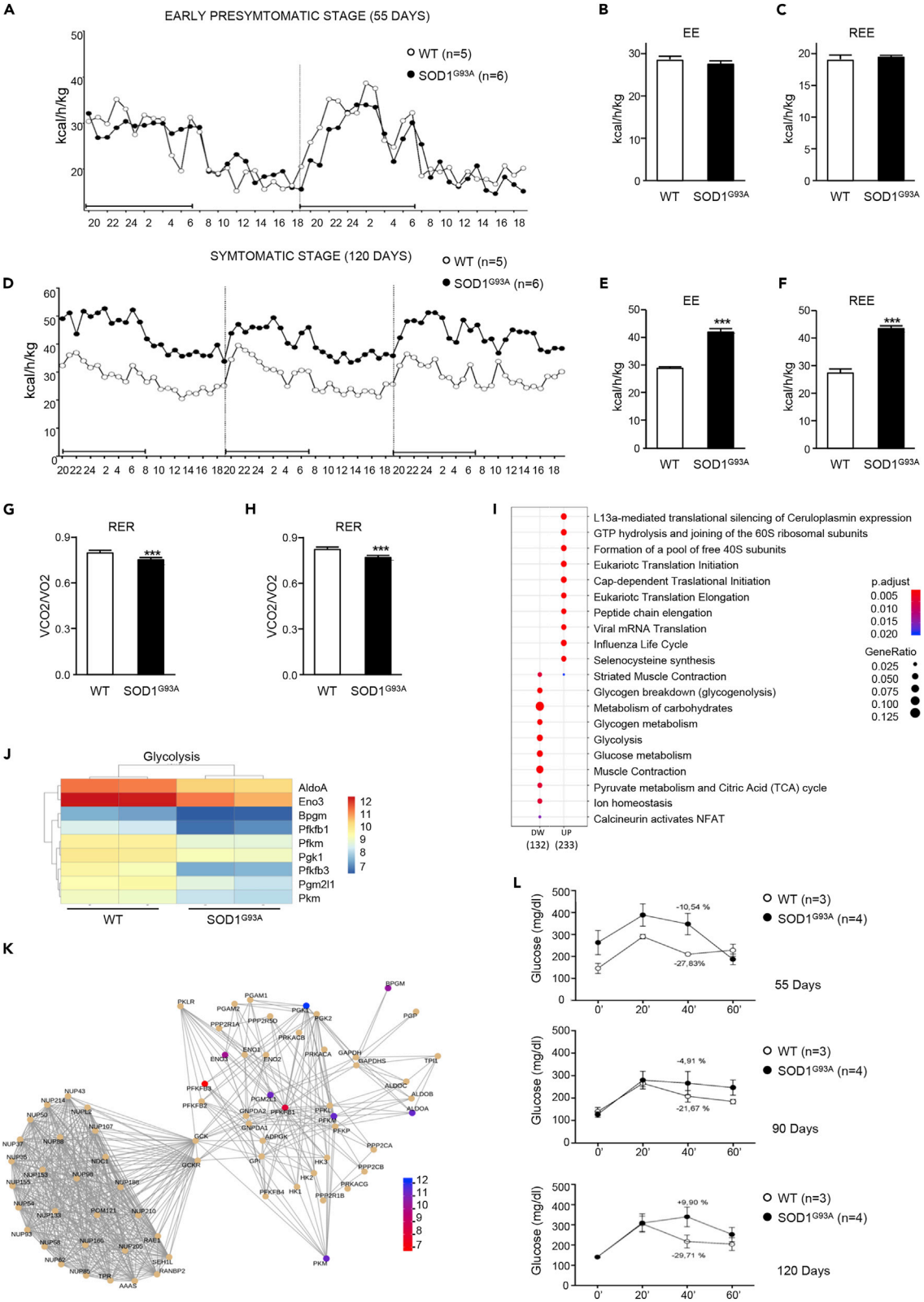
A
EARLY PRESYMTOMATIC STAGE (55 DAYS)
WT (n=5)
SOD1G93A (n=6)
kcal/h/kg
B
EE
C
REE
D
SYMTOMATIC STAGE (120 DAYS)
E
F
G
RER
VCO2/VO2
H
I
L13a-mediated translational silencing of Ceruloplasmin expression
GTP hydrolysis and joining of the 60S ribosomal subunits
Formation of a pool of free 40S subunits
Eukariotc Translation Initiation
Cap-dependent Trasiational Initiation
Eukariotc Translation Elongation
Peptide chain elengation
Viral mRNA Translation
Influenza Life Cycle
Selenocysteine synthesis
Striated Muscle Contraction
Glycogen breakdown (glycogenolysis)
Metabolism of carbohydrates
Glycogen metabolism
Glycolysis
Glucose metabolism
Muscle Contraction
Pyruvate metabolism and Citric Acid (TCA) cycle
Ion homeostasis
Calcineurin activates NFAT
p.adjust
GeneRatio
DW (132)
UP (233)
J
Glycolysis
AldoA
Eno3
Bpgm
Pfkfb1
Pfkm
Pgk1
Pfkfb3
Pgm2l1
Pkm
K
L
Glucose (mg/dl)
-10,54 %
-27,83%
55 Days
-4,91 %
-21,67 %
90 Days
+9,90 %
-29,71 %
120 Days

Figure 1. Energy Expenditure and Metabolic Profile of WT and SOD1^{G93A} Mice

(A–L) (A) Energy expenditure profiles of early presymptomatic SOD1^{G93A} mice (55 days) and their wild-type control littermates (WT). Black bar indicates dark cycle period. Mean (B) energy expenditure (EE) and (C) resting energy expenditure (REE) calculated from (A). (D) Energy expenditure profiles of symptomatic SOD1^{G93A} mice (120 days) and their wild-type control littermates (WT). Mean (E) EE and (F) REE calculated from (D). (G and H) Mean RER from (A) and (D), respectively. (I) Gene expression changes in the tibialis anterior (TA) muscle from SOD1^{G93A} mice and their wild-type control littermates. (J) Heatmap depicting expression of genes from the Reactome category "Glycolysis." Shown genes are differentially expressed with adjusted $p < 0.05$. (K) Network plot of the "Pyruvate metabolism and Citric Acid (TCA) cycle" pathways. Nodes are genes colored based on log2FC, edges are knowledge-based interactions annotated by Reactome. (L) Glucose tolerance test performed in SOD1^{G93A} and in their wild-type control littermates (WT) at 55, 90, and 120 days of age, respectively. Data in (B), (C), (E), (F), (G), and (H) are presented as mean ± SEM, ***$p < 0.0001$, unpaired Student's t test.

2018; Widmann et al., 2019). During endurance training, this metabolic switch is accompanied by an increase in mitochondrial mass alongside significant remodeling of myofibers and a preferential use of fatty acids as fuel (Granata et al., 2018; Widmann et al., 2019). Although we found that mitochondrial mass in glycolytic TA muscle of SOD1^{G93A} mice increased during the disease course, we also noted an early mitochondrial bioenergetic defect. In this regard, we found that total ATP was significantly lower in the TA of SOD1^{G93A} mice at the early symptomatic through to the mid-stage of disease when compared with age-matched wild-type control mice (Figure 3A). Moreover, we observed a marked reduction in all mitochondrial functionalities in the TA of SOD1^{G93A} mice at the early presymptomatic phase of the disease. Similarly, early reductions in mitochondrial function were also observed in other glycolytic muscles, *gastrocnemius* (GNM) and *extensor digitorum longus* (EDL) (Figures S3A and S3B). Interestingly, bioenergetic defects only become detectable in the spinal cord at onset of the pathology (Figures 3C and S3B).

To further investigate the mitochondrial bioenergetic deficit in SOD1^{G93A} mice, we assessed respiration states of mitochondria isolated from skeletal muscle and spinal cord of SOD1^{G93A} mice and wild-type litter matched controls. We observed a decrease in maximally coupled respiration (state 2), thereby confirming the impairment in ATP production. Moreover, maximal respiration (state 4), determined through the addition of the uncoupling agent FCCP, appeared to be significantly compromised in mitochondria obtained from glycolytic TA, GNM, and EDL of presymptomatic SOD1^{G93A} mice (Figures 3B, S3A, and S3B). Interestingly, mitochondria purified from a purely oxidative muscle, the *soleus*, were not affected (Figures S3A and S3B). With the aim of characterizing the alterations in the electron transport chain, we performed a spectrophotometric analysis of the functional activities of the mitochondrial complexes and observed a specific impairment in Complex I in mitochondria purified from the TA (Figure 3D) and GNM (not shown) of early presymptomatic SOD1^{G93A} mice. Again, this dysfunction was evident in skeletal muscle from early presymptomatic SOD1^{G93A} mice, whereas defects in Complex I activity were only observed in the spinal cords of SOD1^{G93A} mice at the symptomatic and end stage of disease (Figure 3E).

Next, we performed Blue Native polyacrylamide gel electrophoresis (BN-PAGE) analysis of digitonin-extracted mitochondrial membranes obtained from the TA of SOD1^{G93A} mice and their wild-type control littermates at different ages (Figure S3C). We found no difference in the assembly of electron transport chain complexes or supercomplexes in mitochondria obtained from SOD1^{G93A} mice when compared with age-matched controls. Finally, bioenergetic assessment of primary cultures of skeletal muscle satellite cells isolated from early presymptomatic SOD1^{G93A} mice (55 days of age) revealed significant decreases in basal respiration, ATP production, maximal respiration, and spare respiratory capacity when compared with those isolated from their wild-type control littermates (Figures 4A and 4B). The decline in maximal respiration and spare respiratory capacity suggests that ALS may inhibit the rapid adaptation of skeletal muscle satellite cells to metabolic changes. Thus, although the number of mitochondria in the whole muscle appears to increase in SOD1^{G93A} mice, mitochondrial metabolism is compromised early in the course of the disease, leading to ATP deficit and impairments in OXPHOS functionality.

Muscle Mitochondrial Deficit in SOD1^{G93A} Mice Occurs in Parallel with an Activation of Molecular Pathways that Compensate for Energy Failure

In normal physiology, a decrease in ATP production (mitochondrial alterations) leads to an enhancement in AMPK activity to promote the binding of AMP (and ADP) to the kinase subunit. This in turn induces the phosphorylation of a wide range of downstream proteins that eventually lead to the activation of catabolic pathways (Hardie et al., 2016). In particular, pharmacological or genetic inhibition of Complex I is sufficient to activate AMPK (Hardie et al., 2016; Thomas et al., 2018). Therefore, in light of the bioenergetic defects

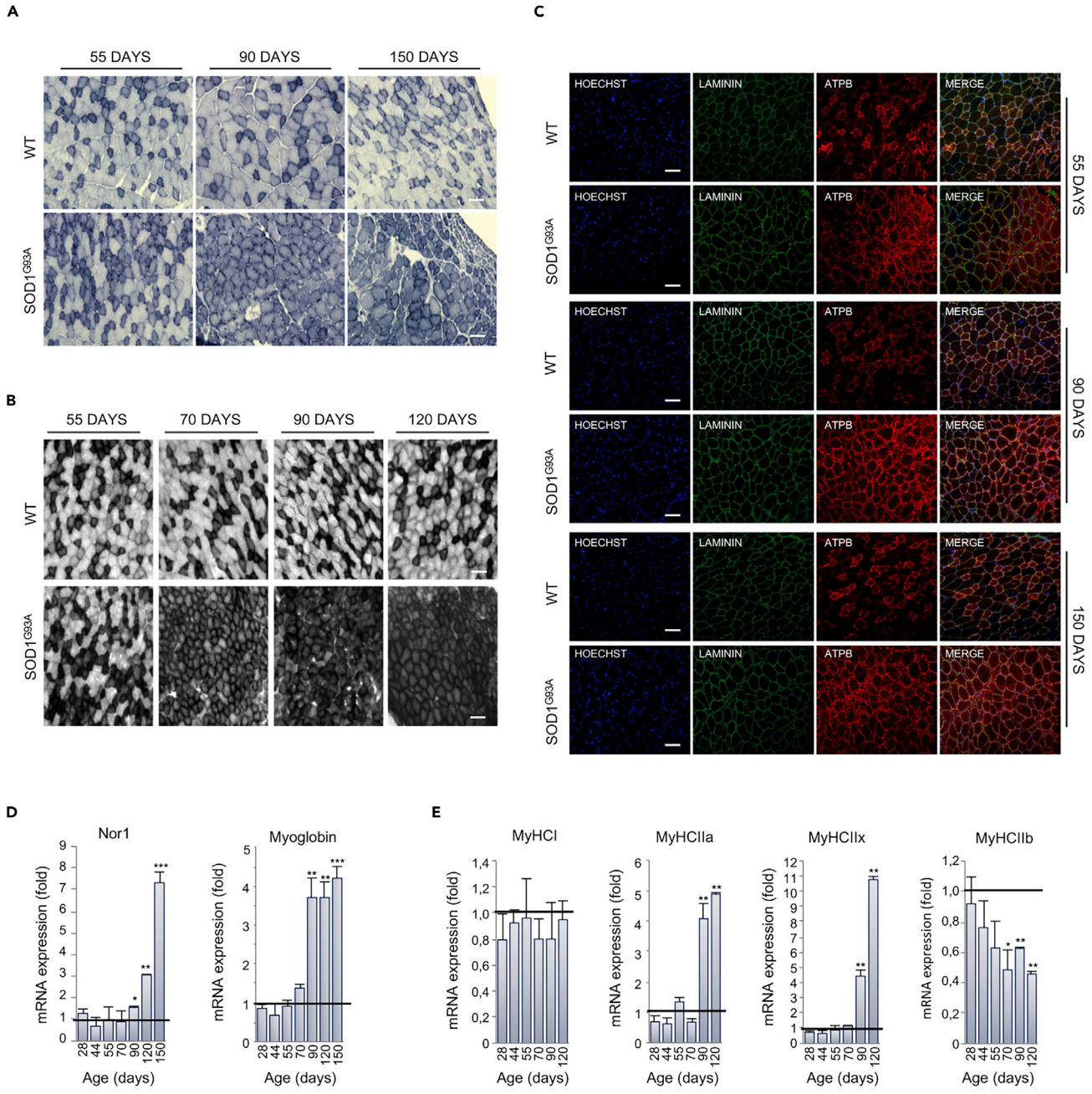

Figure 2. Muscle Metabolism Switches from Glycolytic to Oxidative in SOD1^{G93A} Mice

(A) Representative NADH-tetrazolium reductase activity staining on tibialis anterior (TA) cross sections obtained from 55-, 90-, and 150-day-old SOD1^{G93A} mice and their wild-type control littermates (WT). Scale bar, 100 μm, $n = 3$.

(B) Representative SDH activity staining on TA cross sections of 55-, 70-, 90-, and 120-day-old SOD1^{G93A} mice and their wild-type control littermates (WT). The darker color indicates the site of SDH activity. Scale bar, 100 μm, $n = 3$.

(C–E) (C) Representative images of TA sections from 55-, 90-, and 150-day-old SOD1^{G93A} and wild-type (WT) mice, immunostained with laminin (green) and the mitochondrial marker ATPB (red); nuclei were detected with Hoechst 33342 (blue). Scale bar, 100 μm, $n = 3$. Expression level of mRNAs coding for (D) Nor1 and Myoglobin and (E) MyHCI, MyHCIIa, MyHCIIx, and MyHCIIb in TA sections obtained from SOD1^{G93A} at the indicated ages (at least $n = 4$). Data are presented as mean ± SEM, *$p < 0.05$, **$p < 0.001$, ***$p < 0.0001$, compared with wild-type control littermates at the same age (arbitrarily set at 1), unpaired Student's t test.

Also see Figures S1A–S1C.

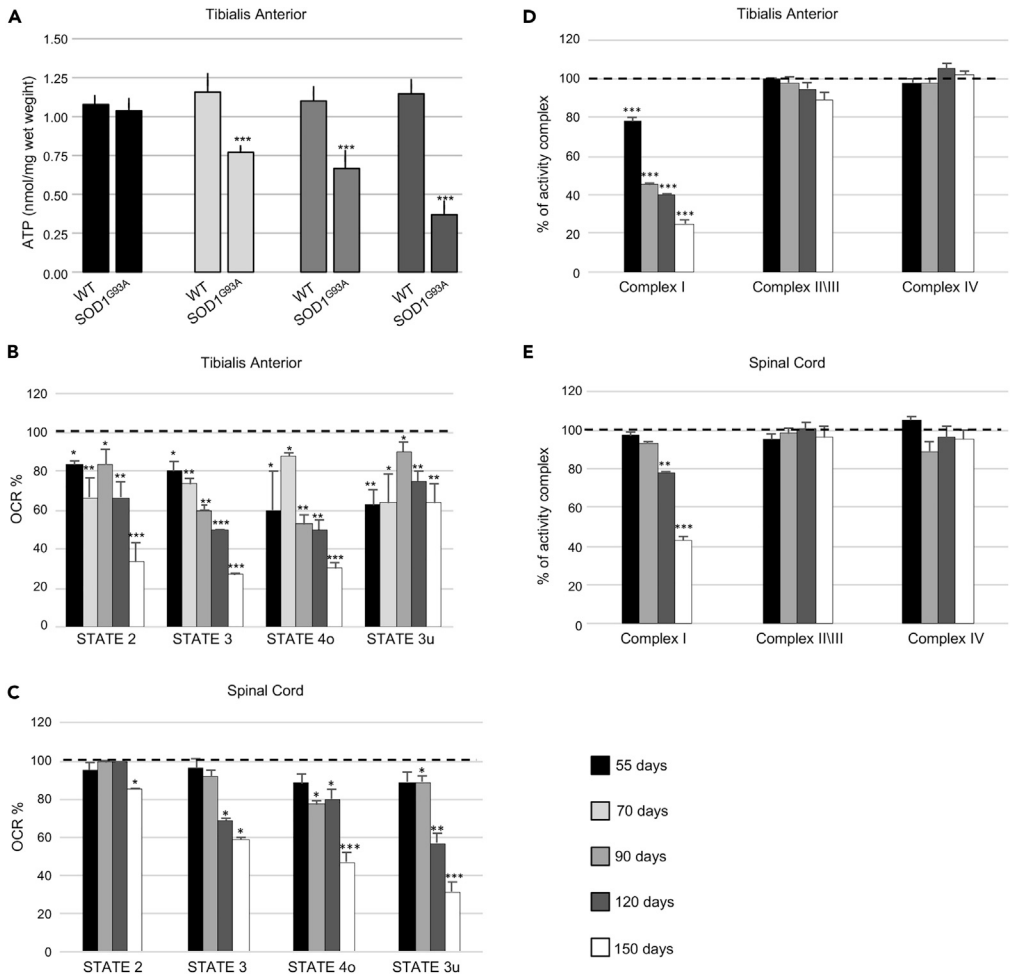

Figure 3. Mitochondrial Bioenergetic Failure Occurs in Skeletal Muscle of Early Presymptomatic SOD1^{G93A} Mice

(A) Fluorometric measurements of total ATP in the tibialis anterior (TA) muscle from SOD1^{G93A} and wild-type age-matched control mice (WT) at different ages. Data were analyzed by unpaired t test and presented as mean ± SEM, ***p < 0.0001 compared with age-matched WT mice (n = 4 independent experiments).

(B) Coupling assay on isolated mitochondria purified from TA.

(C) Spinal Cord of SOD1^{G93A} mice at the indicated ages. Mitochondrial respiration stages are reported as basal respiration (state 2), maximal coupled respiration (state 3), respiration due to proton leak (state 4o), and maximal uncoupled respiration (state 3u). Data are expressed as % Oxygen Consumption Rate (OCR), and 100% was arbitrarily assigned to values obtained from age-matched wild-type mice, *p < 0.05, **p < 0.001, ***p < 0.0001, unpaired Student's t test (n = 5 independent experiments).

(D) Activity of electron transport chain complexes I, II\III, and IV of mitochondria obtained from TA.

(E) Spinal Cord of SOD1^{G93A} and wild-type (WT) mice at the indicated ages. Values were normalized to citrate synthase activity and presented as mean ± SEM, **p < 0.001, ***p < 0.0001 compared with age-matched WT mice (arbitrarily set at 100%), unpaired Student's t test (n = 5 independent experiments).

Also see Figures S2A–S2C and S3A–S3C.

observed in early presymptomatic mice and the specific impairment of Complex I activity, we analyzed the extent of AMPK activation in ALS mice.

Glycolytic skeletal muscles from SOD1^{G93A} mice displayed a robust activation of AMPK, long before the appearance of locomotor symptoms (Figures 5A and S4). AMPK activation occurred in parallel with the phosphorylation/inactivation of the AMPK downstream target Acetyl-CoA Carboxylase (ACC), which catalyzes the first step of fatty acid synthesis (Figures 5A and S4). Moreover, we found an upregulation in carnitine palmitoyltransferase 1 (CPT1) in the skeletal muscle of presymptomatic SOD1^{G93A} mice (Figures 5A

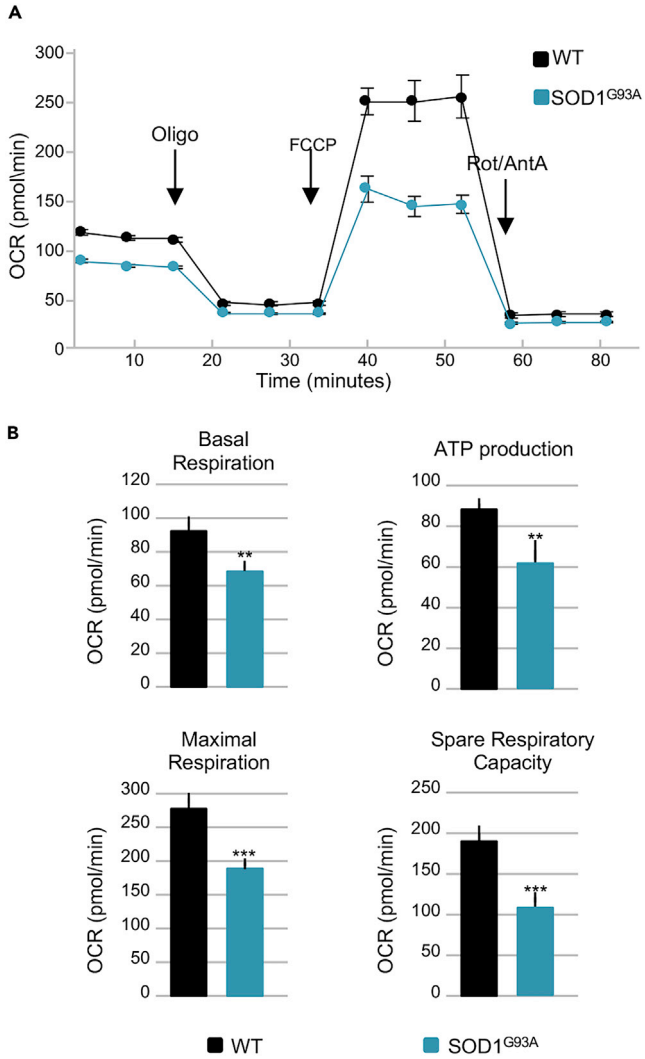

Figure 4. Mitochondrial Bioenergetics Failure Occurs in Skeletal Muscle Satellite Cells Isolated from Early Presymptomatic SOD1^{G93A} Mice

(A) Representative trace of oxygen consumption rate (OCR) in skeletal muscle satellite cells isolated from early presymptomatic SOD1^{G93A} mice (55 days) and their wild-type control littermates (WT).

(B) Individual parameters obtained for basal respiration, ATP production, maximal respiration, and spare respiratory capacity. Each data point represents an OCR measurement. Data are presented as mean ± SEM, **p < 0.001, ***p < 0.0001 relative to WT control, p values obtained from unpaired Student's t test. Data from four independent experiments, with each sample tested in quadruplicate.

and S4). Finally, in support of a metabolic shift toward lipid use, we observed a decrease in the expression of Glucose Transporter type 4 (Glut4) mRNA and the concomitant increase in pyruvate dehydrogenase kinase 4 (Pdk4) mRNA in skeletal muscle of presymptomatic mice (Figure 5B).

Sarcolipin Is an Early Player in ALS Metabolic Alterations

Recent studies have outlined the pivotal role of sarcolipin (SLN) in orchestrating the transition toward oxidative metabolism in skeletal muscle (Maurya et al., 2018). In line with the literature (Babu et al., 2007), we found that SLN is highly expressed in the TA of wild-type control mice until 14 days of age, after which it gradually declines (Figure 6A). By contrast, in SOD1^{G93A} mice, the expression level of SLN remained detectable in TA beyond 14 days of age, increasing during the course of the disease (Figure 6A). Indeed, in SOD1^{G93A} mice, SLN overexpression was strongly upregulated through to the end stage of disease in all glycolytic and oxidative muscles assessed. This is in contrast to the expression profile of SLN in

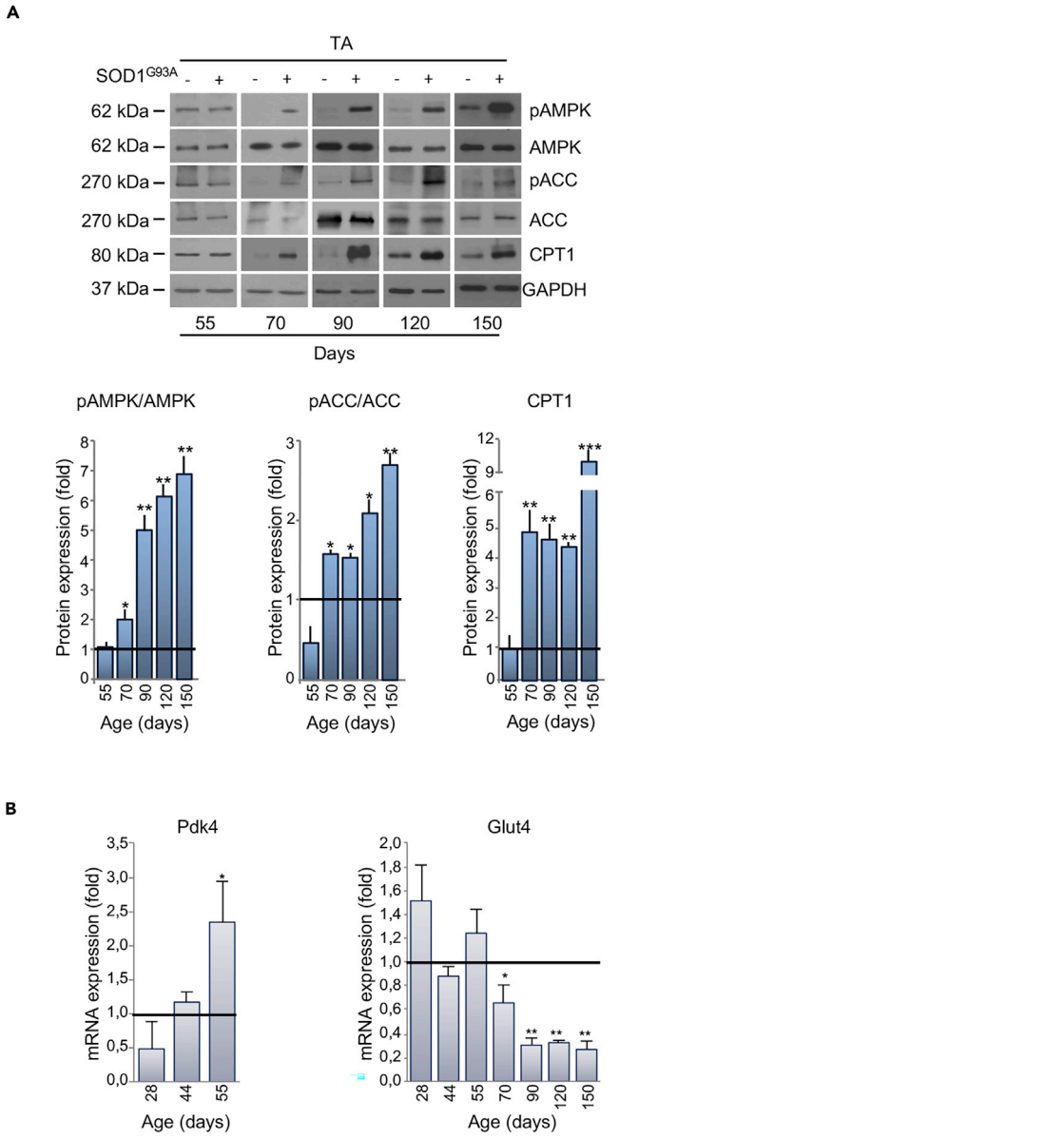

Figure 5. Alterations in Expression of Metabolic Targets Occurs Early in the *tibialis anterior (TA)* of SOD1^{G93A} Mice

(A) Representative western blot images of pAMPK, AMPK, pACC, ACC, and CPT1 (upper panel) in the TA of SOD1^{G93A} and wild-type mice at 55 days of age. GAPDH was used as loading control. Densitometric analysis of pAMPK/AMPK and pACC/ACC ratios and CPT1 expression (lower panel) from $n = 4$ independent experiments.

(B) Expression of mRNAs coding for Pdk4 and Glut4 in the TA of SOD1^{G93A} mice relative to wild-type litter-matched controls. Data presented as mean ± SEM, *$p < 0.05$, **$p < 0.001$, ***$p < 0.0001$ when compared with control littermates at the same age (arbitrarily set at 1), unpaired Student's t test.

Also see Figures S4 and S5A–S5C.

age-matched wild-type control mice, where SLN was only detectable in the oxidative *soleus* (Figure 6B). Of note, we did not observe any significant variation in mRNA expression of phospholamban (PLN) or myoregulin (MLN) (Figure S5A), muscular micropeptides that function similarly to SLN. Thus, our data suggest that SLN is the only SERCA-regulatory micropeptide involved in ALS.

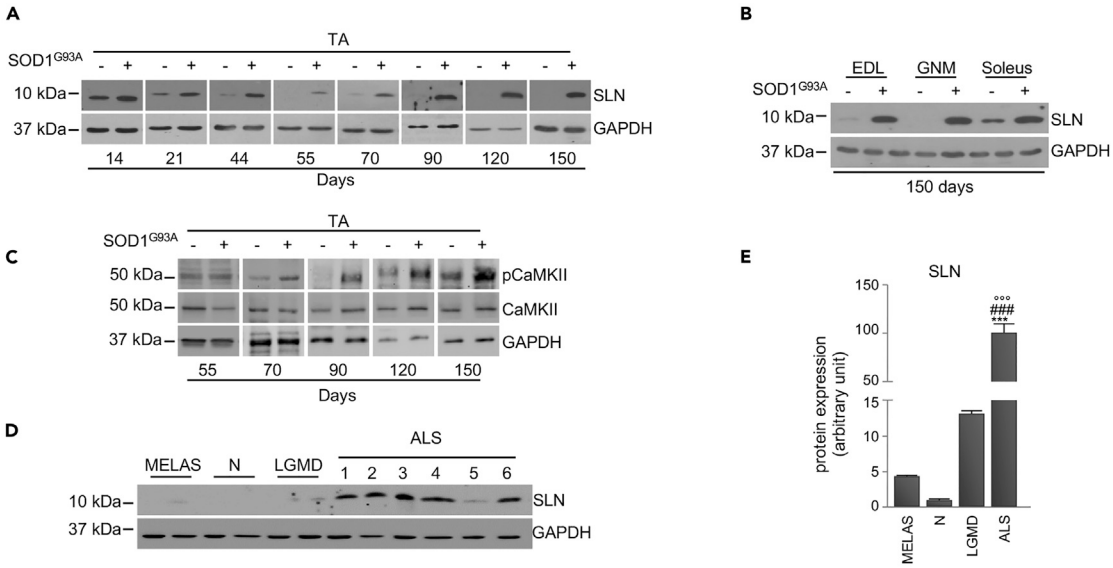
A
TA
SOD1G93A
10 kDa
37 kDa
SLN
GAPDH
14 21 44 55 70 90 120 150
Days
B
EDL GNM Soleus
SOD1G93A
10 kDa
37 kDa
SLN
GAPDH
150 days
C
TA
SOD1G93A
50 kDa
50 kDa
37 kDa
pCaMKII
CaMKII
GAPDH
55 70 90 120 150
Days
D
ALS
MELAS N LGMD 1 2 3 4 5 6
10 kDa
37 kDa
SLN
GAPDH
E
SLN
protein expression (arbitrary unit)
MELAS N LGMD ALS

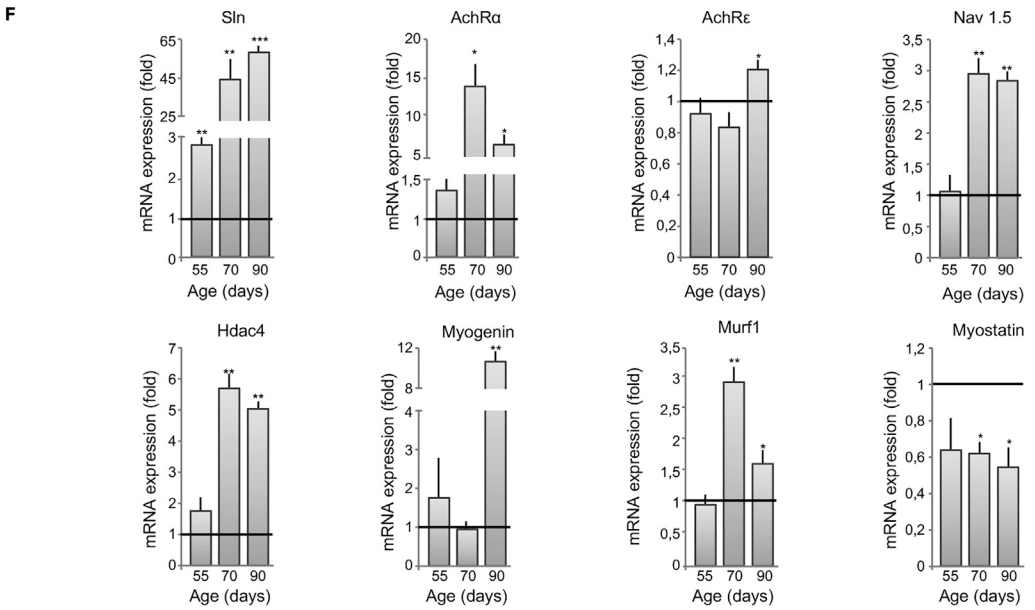
F
Sln
AchRα
AchRε
Nav 1.5
Hdac4
Myogenin
Murf1
Myostatin
mRNA expression (fold)
Age (days)
55 70 90

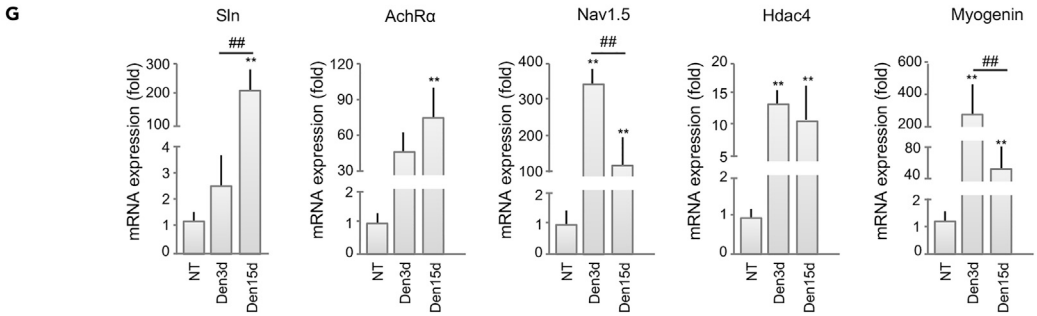
G
Sln
AchRα
Nav1.5
Hdac4
Myogenin
mRNA expression (fold)
NT Den3d Den15d

Figure 6. Upregulation of Sarcolipin in ALS Occurs before Denervation in SOD1^{G93A} Mice

(A and B) Representative western blots of sarcolipin (SLN) protein expression in the (A) tibialis anterior (TA) or (B) Extensor *digitorum longus* (EDL), *gastrocnemius* (GNM), and *soleus* muscle of SOD1^{G93A} (+) and wild-type mice (−) at the indicated ages.

(C) Western blot of pCaMKII and CaMKII in the TA of SOD1^{G93A} (+) and wild type mice (−) at the indicated ages; GAPDH was used as loading control in (A–C).

(D) SLN protein expression in different muscle biopsies derived from MELAS, neuropathy (N), not Limb Girdle Muscle Dystrophy (LGMD) and patients with ALS (1 = SOD1^{D90A} mutation, *soleus*; 2 = sporadic, *vastus lateralis*; 3 = Valosin Containing Protein (VCP) mutation, *vastus lateralis*; 4 = *C9ORF72* repeat expansions, *soleus*; 5 = sporadic, *vastus lateralis*; 6 = sporadic, *rectus femoralis*).

(E) Densitometric analysis of (D) normalized to GAPDH protein expression. Data are presented as a percentage, where an arbitrary value of 100% was assigned to patients with ALS, ***$p < 0.0001$, one-way parametric ANOVA and Tukey's post hoc test.

(F) Expression of mRNAs coding for Sarcolipin (Sln), Acetylcholine Receptor α subunit (Achrα), Acetylcholine Receptor ϵ subunit (Achrϵ), Voltage-gated Na channels 1.5 (Nav1.5), Histone Deacetylase 4 (Hdac4), Myogenin, MuscleRING Finger-1 (Murf1), and Myostatin in the TA of SOD1^{G93A} mice relative to their wild-type control littermates, *$p < 0.05$, **$p < 0.001$ ***$p < 0.0001$ when compared with age control littermates (arbitrarily set at 1).

(G) Expression of mRNAs coding for Sln and denervation markers (Achrα, Nav1.5, Hdac4, and Myogenin) in the TA of wild-type mice 3 and 15 days after sciatic nerve axotomy. Data are expressed as the ratio between the average of values from not axotomized and axotomized mice, *$p < 0.05$, **$p < 0.001$ when compared with control not axotomized mice (arbitrarily set on at 1), and $^{\#\#}p < 0.001$ between mice after 3 and 15 days from axotomy. All data are presented as mean ± SEM, unpaired Student's t test (E) and parametric ANOVA and a Bonferroni post hoc test (F), $n = 3$ or 4 independent experiments.

See also Table 1.

An upregulation in SLN is known to trigger an increase in cytosolic calcium concentration in skeletal muscle (Maurya and Periasamy, 2015). To this end, we found a significant activation of Ca^{2+}/calmodulin-dependent protein kinase II (CaMKII) in skeletal muscle of SOD1^{G93A} at the presymptomatic stage of the disease, when the glycolytic muscle was highly oxidative (Figure 6C). Moreover, we observed a significant increase in PGC-1α protein expression in the TA of SOD1^{G93A} mice at the presymptomatic phase of disease (70 days of age) as well as throughout the course of the disease (Figure S5B).

The expression pattern of mRNAs coding for different isoforms of SERCA pumps reflects the metabolic profile of muscle. SERCA2a and SERCA2b isoforms that are normally associated with oxidative muscle, were more highly expressed in the TA from SOD1^{G93A} mice, whereas the glycolytic muscle-associated SERCA1 isoform was downregulated at the presymptomatic stage (Figure S5C). It is noteworthy that SLN selectively binds SERCA2 isoforms, interacting with these to trigger the transition of skeletal muscle from glycolytic to oxidative metabolism (Anderson et al., 2016). Finally, highly relevant was the finding that SLN expression was upregulated in muscle biopsies obtained from six patients affected by different forms of ALS (for details see Table 1). Indeed, all ALS biopsies showed higher expression levels of SLN when compared with control patients affected by other muscular disorders (Figures 6D and 6E).

Sarcolipin Overexpression in SOD1^{G93A} Mice Is Not Related to Muscle Denervation

Several pathological conditions that lead to skeletal muscle disuse and subsequent atrophy affect not only muscle mass but also muscle metabolism (Tintignac et al., 2015). SLN has been described to be a key mediator of metabolic modifications occurring in unloaded/disused muscle (Fajardo et al., 2017). Thus, to discriminate whether SLN upregulation is causally linked to the altered metabolic state observed in ALS mice, or whether it is merely a consequence of early denervation, we analyzed the expression levels of several denervation/atrophy markers. Our results demonstrate that, in TA from SOD1^{G93A} mice, SLN is upregulated at the early presymptomatic stage, whereas mRNAs coding for Hdac4, Nav1.5, Myogenin, AchRε, AchRα, Murf1, and Myostatin, all associated with the denervation process, are only increased at the later stages of disease (Figure 6F).

In order to further decipher the relationship between denervation and metabolic alterations in skeletal muscle from ALS mice, we used an experimental paradigm of acute denervation. As shown in Figure 6G, sciatic nerve axotomy in control mice evoked an upregulation in denervation markers after 3 days, whereas SLN was only found to increase after 15 days. Overall, our data strongly suggest that, in ALS, muscle metabolic reprogramming is orchestrated by SLN and this occurs independent of denervation.

Altered Muscle Performance in SOD1^{G93A} Mice Is Related to Hypermetabolism

Given the altered bioenergetic profiles observed in SOD1^{G93A} mice, we next tested whether pharmacological targeting of altered energy metabolism could be a beneficial therapeutic approach in ALS. To address this aim, we chronically administered ranolazine (RAN) to SOD1^{G93A} mice. RAN is a US Food and Drug Administration (FDA)-approved drug that is used to treat ventricular hypertrophy, and it has been shown to exert cardioprotective effects by facilitating higher energy production under conditions of lower oxygen

Patient	Age (years)	Sex	ALS Mutation	Months from Diagnosis	Muscle (Biopsies Were Done on Limb Muscle where the Disease Began)	Patient Information
1	47	F	$SOD1^{D90A}$	12	*soleus dx*	Spinal onset
2	72	F	Sporadic	42	*vastus lateralis dx*	Spinal onset
3	50	M	VCP mutation	54	*vastus lateralis dx*	Spinal onset with IBM (inclusion body myositis) and Paget's disease
4	62	F	C9ORF72 (58 repeats)	33	*soleus dx*	Spinal onset with progressive muscle atrophy
5	77	F	Sporadic	19	*vastus lateralis dx*	Spinal onset
6	71	F	Sporadic	14	*rectus femoris dx*	N/A

Table 1. Demographics of Patients with ALS

supply (Stanley, 2002). This drug decreases β-oxidation, thereby restoring the use of glucose as fuel (McCormack et al., 1998).

In a preliminary dose-response study, a small cohort of $SOD1^{G93A}$ mice and age-matched wild-type control mice received daily intraperitoneal (i.p.) injections, for seven consecutive days, of three different doses of RAN (25, 50, 100 mg/kg). Treatment commenced at an age that corresponds to the symptomatic stage of the disease in $SOD1^{G93A}$ mice (110 days). Bioavailability of RAN in plasma was assessed by high-performance liquid chromatography (HPLC), and results confirmed a dose-dependent increase (Table 2). RAN concentration values were consistent with those registered in more extended pharmacokinetics and pharmacodynamics studies reported by others (Patel and Hasumati, 2015). Analysis of grip strength and SLN expression were used as readouts to determine the efficacy of RAN treatment. Strikingly, $SOD1^{G93A}$ mice receiving 50 and 100 mg/kg of RAN showed a marked increase in muscular strength after 2 days of treatment. This improvement was maintained throughout the 7-day treatment period (Figure S6A). Similar results were obtained with a lower dose of RAN (25 mg/kg), which showed a significant, although delayed, efficacy. Furthermore, in the TA muscle of $SOD1^{G93A}$ mice, SLN expression was reduced after 7 days of treatment. This was most evident at a RAN dose of 50 mg/kg (Figure S6B). As such, 50 mg/kg of RAN was selected as the most effective dose.

A second, larger cohort of $SOD1^{G93A}$ mice received 50 mg/kg RAN from the onset stage of disease (90 days) through the end stage of disease. As shown in Figure 7A, RAN treatment improved hanging grid performance in $SOD1^{G93A}$ mice up until the fully symptomatic stage of the disease (132 days). However, this improvement was not sustained; hanging grid performance in RAN-treated $SOD1^{G93A}$ mice was comparable with that of non-treated $SOD1^{G93A}$ mice by the end stage of disease (Figure 7A). Interestingly, RAN exerted similar effects on wild-type mice (Figure S7). Despite improving hanging grid performance in $SOD1^{G93A}$ mice, RAN failed to improve survival (Figure 7B) and it did not provide weight changes (data not shown). Interestingly, RAN treatment improves glycemia and reverses glucose intolerance in murine models of metabolic alterations without modifying body weight development (Batran et al., 2019; Ning et al., 2011).

It is noteworthy that treatment efficacy followed the trend of expression/activation of muscle metabolic markers. Indeed, after 30 days of treatment with RAN, SLN was markedly downregulated and CaMKII and AMPK were inactivated by dephosphorylation, whereas the AMPK target, ACC, was dephosphorylated and hence reactivated (Figures 8A and 8B). Similarly, expression levels of mRNAs encoding myosin subtypes and SERCA pumps were decreased in response to RAN (Figure 8C), whereas mRNAs encoding Nor1 and Glut4 returned to levels similar to that observed in wild-type control mice (Figure 8C). In line

RAN Dose (mg/kg)	WT (μM)	SOD1^{G93A} (μM)
25	0.63 ± 0.16	0.79 ± 0.11
50	1.22 ± 0.20	1.30 ± 0.18
100	3.33 ± 0.21	2.87 ± 0.17

Table 2. HPLC Determination of Ranolazine (RAN) Plasma Concentrations 12 h after i.p. Administration of Ranolazine at 25, 50, or 100 mg/kg

Data are expressed as mean ± SD, n = 5 per group.

with RAN's known mechanism of action in improving glucose metabolism, fluorometric determination of total ATP content showed a net increase in ATP concentration in the TA from symptomatic, 120-day-old SOD1^{G93A} mice when compared with their wild-type control littermates (Figure 8D).

Given that progressive changes in muscle metabolic markers in SOD1^{G93A} mice occurred alongside the presentation of hypermetabolism, we next aimed to determine whether RAN would attenuate hypermetabolism in SOD1^{G93A} mice. Indeed, indirect calorimetry analysis showed that hypermetabolism was partially abrogated after treatment with RAN (Figures 8E and 8F). RAN restored EE (Figure 8G) and REE (Figure 8H) but had no effect on RER (Figure 8I). Surprisingly, the weakening of RAN effects during the end stage of the disease was paralleled with an increase in the expression of SLN, the reactivation of CaMKII and AMPK, and thus ACC inactivation (Figures 8, 8J, and 8K). Overall, these results show that decreasing EE is linked to an improvement in grip strength in SOD1^{G93A} mice. Our data highlight the potential relevance of pharmacological interventions aimed at counteracting hypermetabolism in ALS.

DISCUSSION

In this study, we detail the existence of early events responsible for the remodeling of myofiber-type composition and defective energy metabolism in the SOD1^{G93A} mouse model of ALS. Our observations are in agreement with previous work demonstrating a shift in fast-to-slow muscle fiber type composition (Peggion et al., 2017), as well as aberrant mitochondrial metabolism (Salvatori et al., 2017) and alterations in muscle glucose metabolism in response to muscle-restricted overexpression of SOD1^{G93A} (Dobrowolny et al., 2008, 2018). Moreover, in line with the derangement in whole-body EE that we identified in symptomatic SOD1^{G93A} mice, hypermetabolism has been described in many patients with ALS (Bouteloup et al., 2009; Desport et al., 2005; Funalot et al., 2009; Jésus et al., 2018; Steyn et al., 2018) and often associated with dyslipidemia (Dupuis et al., 2008). Notably, prognosis is less favorable in hypermetabolic patients (Steyn et al., 2018), whereas dyslipidemia/hyperlipidemia may confer protection and increase survival (Dupuis et al., 2008).

Given that skeletal muscle is a major determinant of whole-body energy metabolism (Zurlo et al., 1990), we focused our investigation on the contribution of skeletal muscle to SOD1^{G93A} metabolic dysfunction. Indeed, we found some prodromal molecular signatures of oxidative metabolism at 55 days of age, including an initial increase in NADH-TR and SDH activities and an increase in mitochondrial mass in fast-twitch glycolytic muscles. Thus, we identified a fast-to-slow skeletal muscle fiber transition in the early presymptomatic stage; this pathological rearrangement of muscle phenotype might partially account for the marked increase of fatty acid β-oxidation observed before disease onset. However, according to previous evidence (Doshi et al., 2017), hypermetabolism occurs in SOD1 G93A mice only at a symptomatic stage of the disease, whereas it is undetectable at 55 days of age. It should be considered that, around 55 days of postnatal life, the skeletal muscle of SOD1 G93A mice are not yet fully oxidative.

Skeletal muscle is a dynamic tissue that is highly adaptable to environmental changes and to alterations in energy need. Physical exercise is a key modulator of muscle plasticity, as enduring contractile activity, it is a powerful stimulus for enhancing mitochondrial biogenesis (Hood, 2009). This condition upregulates mitochondrial enzymes involved in fatty acid β-oxidation (Lundsgaard et al., 2018) to promote myofiber switching from fast (glycolytic) to slow (oxidative) fiber types (Flück, 2006). In this view, the muscle alterations that we have observed in SOD1^{G93A} mice appear to mimic a state of long-lasting endurance exercise. Indeed, Palamiuc et al. (2015) have previously reported increased endurance capacity in SOD1^{G86R} mice at an advanced phase of disease. Although it remains unknown as to why

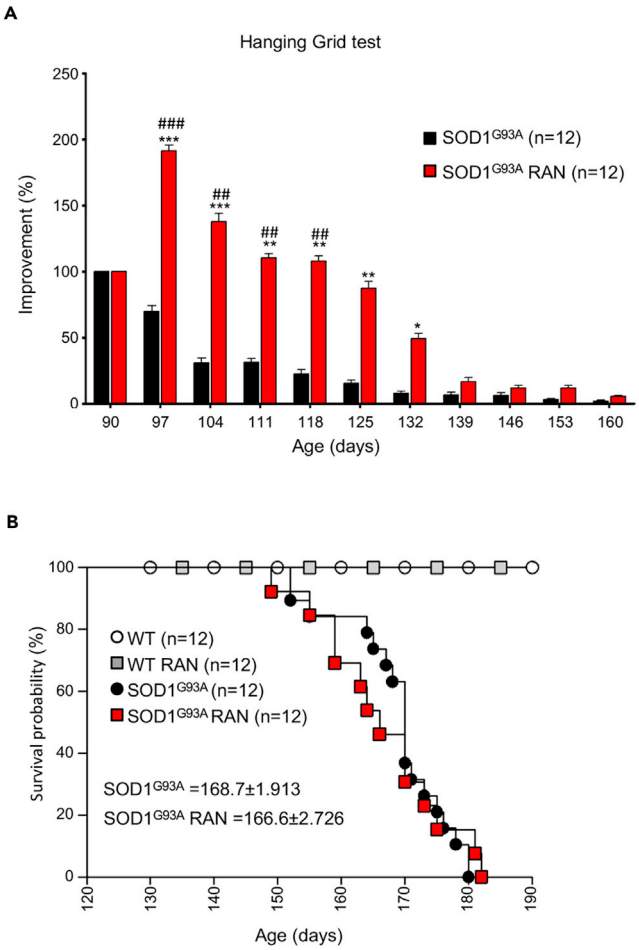

Figure 7. Ranolazine Improves Locomotor Abilities but Does Not Affect Survival

(A) Locomotor abilities of SOD1^{G93A} mice receiving daily intraperitoneal injections of Ranolazine 50 mg/kg (SOD1^{G93A} RAN) or physiological solution (SOD1^{G93A}) evaluated by hanging grid test at the indicated days. Performance was evaluated from 90 days of age (start of treatment) to the end stage of disease. Data are presented as mean ± SEM, *p < 0.05 **p < 0.001 ***p < 0.0001 when compared with age-matched SOD1^{G93A} untreated mice, and $^{\#}$p < 0.05 $^{\#\#}$p < 0.01 $^{\#\#\#}$p < 0.0001 when compared with SOD1^{G93A} mice at the beginning of treatment. (n = 12 SOD1^{G93A}, n = 12 SOD1^{G93A} + RAN).

(B) Kaplan-Meier survival curve of SOD1^{G93A} mice and their wild-type control littermates (WT) receiving daily intraperitoneal injections of Ranolazine 50 mg/kg (SOD1^{G93A} RAN and WT RAN) or physiological solution (SOD1^{G93A} and WT). p Values were obtained using parametric two-way ANOVA with Bonferroni post hoc test (A) or one-way ANOVA with Bonferroni post hoc test (B).

Also Figure S7.

there is a shift in muscle fiber type, and enhanced fatty acid utilization in the absence of environmental pressure and/or physical exercise in SOD1^{G93A} mice, this exercise-mimetic phenotype may be associated with aberrant energy needs that may be associated with early mitochondrial dysfunction and/or SLN overexpression.

Mitochondrial Dysfunction

In light of the critical role that mitochondria play in muscle metabolism and plasticity, it is conceivable that early alterations in muscle mitochondria might contribute to altered energy homeostasis in ALS. In agreement with this hypothesis, we report mitochondrial impairments in skeletal muscle in early presymptomatic SOD1^{G93A} mice, which occur prior to the presentation of motor symptoms. Recently, an association between myopathy and defective mitochondrial function has been described in a different ALS mouse model

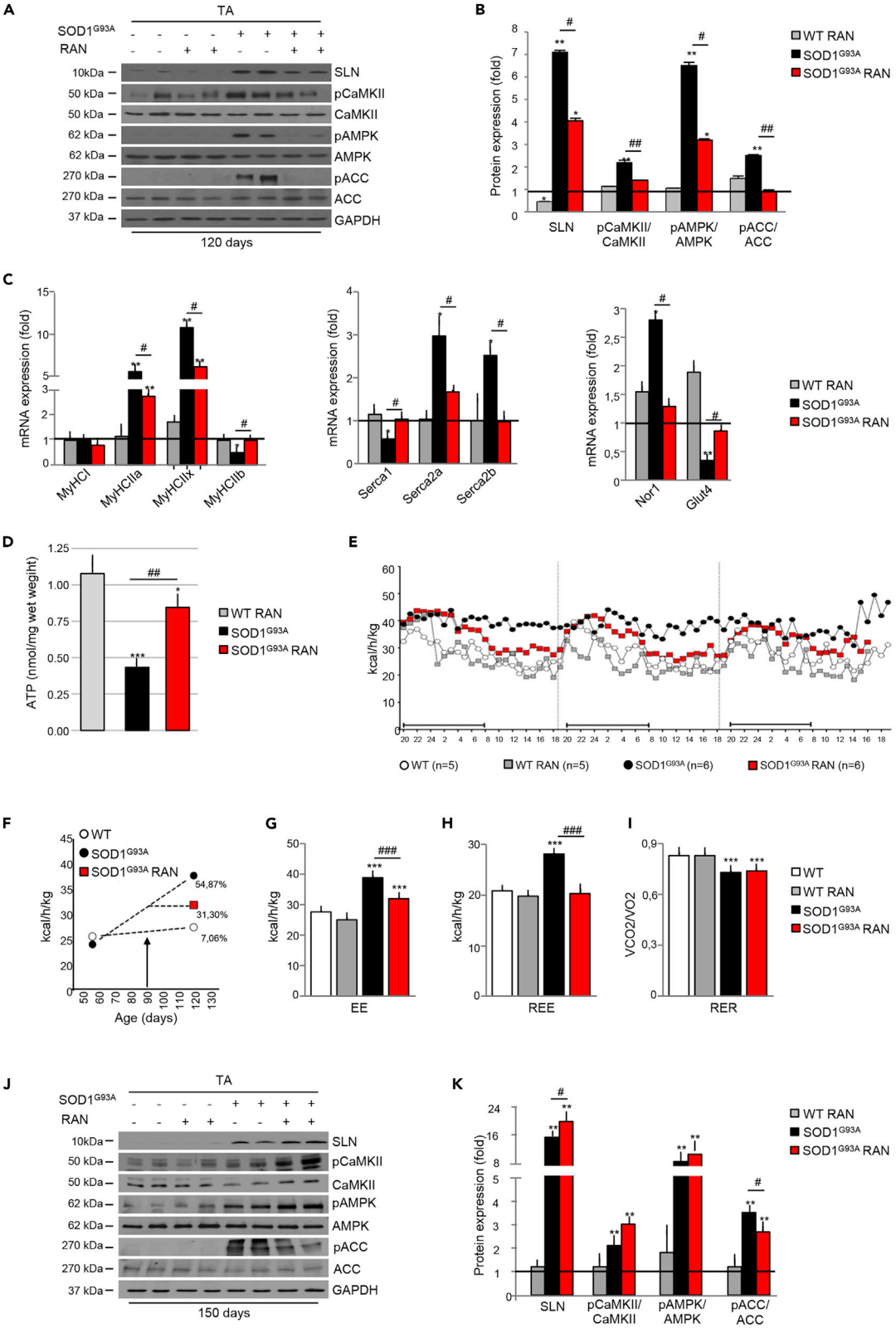
A
TA
SOD1G93A
RAN
10kDa
50 kDa
50 kDa
62 kDa
62 kDa
270 kDa
270 kDa
37 kDa
SLN
pCaMKII
CaMKII
pAMPK
AMPK
pACC
ACC
GAPDH
120 days
B
Protein expression (fold)
SLN
pCaMKII/ CaMKII
pAMPK/ AMPK
pACC/ ACC
WT RAN
SOD1G93A
SOD1G93A RAN
C
mRNA expression (fold)
MyHCI
MyHCIIa
MyHCIIx
MyHCIIb
Serca1
Serca2a
Serca2b
Nor1
Glut4
WT RAN
SOD1G93A
SOD1G93A RAN
D
ATP (nmol/mg wet weight)
WT RAN
SOD1G93A
SOD1G93A RAN
E
kcal/h/kg
WT (n=5)
WT RAN (n=5)
SOD1G93A (n=6)
SOD1G93A RAN (n=6)
F
WT
SOD1G93A
SOD1G93A RAN
54,87%
31,30%
7,06%
kcal/h/kg
Age (days)
G
kcal/h/kg
EE
H
kcal/h/kg
REE
I
VCO2/VO2
RER
WT
WT RAN
SOD1G93A
SOD1G93A RAN
J
TA
SOD1G93A
RAN
10kDa
50 kDa
50 kDa
62 kDa
62 kDa
270 kDa
270 kDa
37 kDa
SLN
pCaMKII
CaMKII
pAMPK
AMPK
pACC
ACC
GAPDH
150 days
K
Protein expression (fold)
SLN
pCaMKII/ CaMKII
pAMPK/ AMPK
pACC/ ACC
WT RAN
SOD1G93A
SOD1G93A RAN

Figure 8. Chronic Ranolazine (RAN) Administration Restores Metabolic Homeostasis

Mid-term evaluation (120 days) of SOD1^{G93A} mice receiving daily RAN (50 mg/kg i.p.) from 90 days of age.

(A) Western blot analysis of SLN, pCaMKII, CaMKII, pAMPK, AMPK, pACC, and ACC in the tibialis anterior (TA) of SOD1^{G93A} mice (+) and wild-type control littermates (−) receiving daily RAN (+) or vehicle (−) at 120 days of age. GAPDH was used as loading control.

(B) Densitometric analysis of data obtained in (A). Data are presented as mean ± SEM, *p < 0.05, **p < 0.001 when compared with wild-type untreated mice (arbitrarily set on at 1) and $^{\#}$p < 0.05 $^{\#\#}$p < 0.001 when compared with SOD1^{G93A} untreated mice (n = 6 independent experiments), parametric one-way ANOVA and a Bonferroni post hoc test.

(C) Expression of mRNAs coding for Nor1, Glut4, Serca1, Serca2a, Serca2b, MyHCI, MyHCIIa, MyHCIIx, MyHCIIb in the TA of SOD1^{G93A} mice and wild-type control littermates treated with RAN (SOD1^{G93A,} RAN and WT RAN) or not treated with RAN (SOD1^{G93A} and WT) at 120 days of age (n = 4 for each genotype/treatment). Data are presented as mean ± SEM, **p < 0.001 when compared with wild-type untreated mice (arbitrarily set on at 1) and $^{\#}$p < 0.05 when compared with SOD1^{G93A} untreated mice (n = 6 independent experiments), parametric one-way ANOVA and a Bonferroni post hoc test.

(D) Fluorometric measurement of total ATP in the TA of SOD1^{G93A} mice and wild-type control littermates receiving daily RAN (+) or vehicle (−) at 120 days of age. Data were analyzed by one-way ANOVA with multiple comparisons using Dunnet's t test and Tukey's HSD (Honestly Significantly Different) post hoc test. Data presented as mean ± SEM, ***p < 0.0001 when compared with WT untreated mice and $^{\#\#}$p < 0.001 when compared with SOD1^{G93A} untreated mice (n = 4 independent experiments).

(E) Energy expenditure profile (EE) of WT and SOD1^{G93A} treated with RAN or vehicle at 120 days of age. Black bar indicates the dark cycle period.

(F–H) (F) Percentage of increase in EE between 55 and 120days of age, and effects of RAN treatment (initiation of treatment marked with an arrow) from day 90 onward. Mean of (G) EE and (H) Resting EE (REE) obtained from WT and SOD1^{G93A} mice in (E). Data are presented as mean ± SEM, ***p < 0.0001 when compared with WT mice; $^{\#\#\#}$p < 0.0001 when compared with SOD1^{G93A} mice (at least n = 4 animals), two-way ANOVA with Tukey post hoc test.

(I–K) (I) Respiratory exchange ratio (RER) demonstrating the extent of lipid versus carbohydrate oxidation. Data are presented as mean ± SEM, ***p < 0.0001 when compared with WT mice; (at least n = 4 animals), two-way ANOVA with Tukey post hoc test. Long-term evaluation (150 days) of RAN treatment started at 90 days of age: (J) western blot analysis of SLN, pCaMKII, CaMKII, pAMPK, AMPK, pACC, and ACC in the TA of SOD1^{G93A} (+) and wild-type (−) RAN-treated (+) or untreated (−) mice. GAPDH was used as loading control. (K) Densitometric analysis of data in (I). Data are presented as mean ± SEM, **p < 0.001 when compared with WT untreated mice (arbitrarily set on at 1) and $^{\#}$p < 0.05 when compared with SOD1^{G93A} untreated (n = 6 independent experiments), parametric one-way ANOVA and a Bonferroni post hoc test.

(Genin et al., 2019), thus underlining the importance of muscle bioenergetics in neuron motor disease. In line with premature atrophy and loss of function of fast-twitch fibers (Hegedus et al., 2008; Palamiuc et al., 2015; Peggion et al., 2017), we detected early mitochondrial metabolic alterations in glycolytic EDL, TA, and GNM but not in oxidative *soleus*. Interestingly, skeletal muscle satellite cells isolated from early pre-symptomatic SOD1^{G93A} mice also exhibited defective bioenergetic profiles. The drop in energy production in these skeletal muscle stem cells and their inability to respond to metabolic changes might affect muscle regeneration in response to denervation as previously described in ALS pathology (Tsitkanou et al., 2016; Yin et al., 2013).

We found an early impairment of Complex I activity in skeletal muscle of SOD1^{G93A} mice. An impairment of Complex I activity has previously been described in muscle biopsies from patients with sporadic ALS (Wiedemann et al., 1998). Moreover, functional alterations of the Complex I has been observed in GNM isolated from SOD1^{G93A} mice at 7 weeks of age (Capitanio et al., 2012). Collectively, these observations corroborate the hypothesis that, in patients with ALS (Ghiasi et al., 2012) and in preclinical models (Salvatori et al., 2018; Wang et al., 2016), Complex I activity is a selective target of different ALS-related proteins. Complex I can be considered as an energy-transducing enzyme whose activity regulates cell energy request and activates catabolic pathways following the failure of its activity (Hunter et al., 2018; Leonard et al., 2017). Accordingly, pharmacological inhibition or a failure in Complex I activity triggers the activation of the AMPK (Hu et al., 2017; Hunter et al., 2018). AMPK activation promotes catabolic pathways, such as lipid oxidation in skeletal muscle (Merrill et al., 1997; O'Neill et al., 2013). This known action of AMPK is in line with the increase in lipid oxidation and inhibition of glucose utilization that we observed here in early presymptomatic mice. In the context of ALS, mitochondrial failure could drive an increase in the use of lipids as primary fuel substrate to compensate for energy deficit and a decline in ATP synthesis. Subsequent to this, excess ROS generation as a result of excessive mitochondrial lipid oxidation may further aggravate mitochondrial dysfunction (Quijano et al., 2016; Rosca et al., 2012).

SLN Overexpression

SLN is a micropeptide inhibitor of SERCA activity that uncouples Ca^{2+} transport from ATP hydrolysis (Bal et al., 2012; Smith et al., 2002). Thus, SLN has a critical role in determining metabolic rate, EE, and muscle-derived thermogenesis (Bal et al., 2012; Maurya and Periasamy, 2015; Maurya et al., 2018). Notably, selective SLN overexpression in fast-twitch glycolytic muscle has been shown to reprogram mitochondria and induce an oxidative phenotype (Maurya et al., 2018). The expression of SLN is tightly regulated during development, and in rodents, its expression is detectable in skeletal muscle during late embryonic

development and early neonatal life (Babu et al., 2007). Accordingly, in control mice SLN expression was downregulated in glycolytic muscle by postnatal day 15, whereas its expression was highly upregulated in the same muscle during the entire life course of SOD1^{G93A} mice. More interestingly, we found marked SLN overexpression in muscle biopsies from patients affected by genetic and sporadic forms of ALS. Although SLN has already been viewed as a feasible prognostic or early diagnostic biomarker in ALS, its upregulation has been associated with disease-specific denervation (Calvo et al., 2012) rather than specific metabolic signatures. In contrast to this, our results indicate that SLN is overexpressed before the upregulation of any denervation markers. Although our data do not pinpoint SLN upregulation as being the primary "source" of hypermetabolism in ALS, early mitochondrial failure and energy deficit could underlie SLN overexpression and activate compensatory oxidative metabolism. Indeed, SLN plays a central role in the adaptive mechanisms that couple increased energy request (e.g., diet-induced obesity), cold acclimatization, and exercise with mitochondrial ATP and energy production (Maurya et al., 2018). Thus, the increase of SLN expression in ALS might represent a classical adaptation to increased energy demand, leading to a shift in substrate utilization, mitochondrial biogenesis, and oxidative metabolism in glycolytic muscle.

RAN Treatment

To determine whether decreasing energy demand and re-balancing substrate utilization might be of benefit in ALS, we aimed to assess the potential therapeutic role of RAN, an FDA-approved fatty acid oxidation inhibitor that is used for the management of cardiac dysfunction (Bhandari and Subramanian, 2007; Stanley, 2002). We demonstrate that chronic RAN treatment in SOD1^{G93A} mice significantly improves motor function in SOD1^{G93A} by slowing the decline in muscle strength over a 6-week treatment period. Moreover, during mid-term treatment evaluation (120 days of age), we found that RAN attenuated excessive whole-body EE in SOD1^{G93A} mice, and although it did not offset increased fatty acid β-oxidation, RAN treatment improved energy metabolism by increasing muscle ATP content.

Interestingly, we found that, by the end stage of disease (at 150 days), RAN had lost its efficacy and there was a re-emergence of hypermetabolism. It should be noted that, in patients with stable angina pectoris, the recommended posology includes the escalation of drug dosage during therapy (www.ema.europa.eu/ema/index.jsp?curl=pages/medicines/human/medicines/000805/human_med_001009.jsp&mid=WC0b01ac058001d124). This suggests that the re-emergence of pathology at the end stage of disease in SOD1^{G93A} mice may be attributed to the loss of RAN efficacy rather than disease exacerbation. Of interest, RAN also acts as an inhibitor of late inward sodium currents (IpNa) during cardiac repolarization (Belardinelli et al., 2013). Hence, we cannot rule out that sodium channel facilitation of membrane repolarization might decrease cell energy demand to compensate for mitochondrial failure in skeletal muscle and neurons of SOD1^{G93A} mice.

Conclusions

Our study provides compelling evidence to demonstrate specific metabolic dysfunction and mitochondrial failure as early pathophysiological events in ALS. Here, we may consider that a slight drop in ATP production via mitochondrial impairment or SLN overexpression may become pathologically relevant when energy demand increases as a result of lifestyle changes or during aging. In this scenario, a timely pharmacological intervention impinging on hypermetabolism may be a promising therapeutic option to improve quality of life.

Limitations of the Study

In this study we use an FDA-approved drug, Ranolazine, to counteract hypermetabolism in an ALS mouse model. In our hands, Ranolazine ameliorates locomotor symptoms of fully symptomatic ALS mice, but its effect is temporary. In this regard, RAN does not improve life span in SOD1^{G93A} mice. Given that we have observed temporary restoration and recovery of metabolic indicators, the loss of effectiveness of Ranolazine requires further investigation through extended pharmacokinetics and pharmacodynamics studies. From our study, we provide proof of concept that hypermetabolism appears to be considered a viable therapeutic target in ALS. As such, alternate drugs that are known to modulate metabolism should also be considered.

METHODS

All methods can be found in the accompanying Transparent Methods supplemental file.

SUPPLEMENTAL INFORMATION

Supplemental Information can be found online at https://doi.org/10.1016/j.isci.2020.101087.

ACKNOWLEDGMENTS

This work was supported by AriSLA through HyperALS project (A.F.); AFM-Telethon project n. 2018; AFM-Telethon project n. 21021 (J.P.L. and A.F.); the National Health and Medical Research Council (1101085 and 1185427 to F.J.S. and S.T.N.); Scott Sullivan MND Research Fellowship (Queensland Brain Institute, the Royal Brisbane & Women's Hospital Foundation, The MND and Me Foundation) (S.T.N.); and Australian Institute for Bioengineering and Nanotechnology (S.T.N.).

This work is dedicated to the memory of our dear Mentor and Friend Maria Teresa Carrì.

AUTHOR CONTRIBUTIONS

S.S. and I.S. designed and performed experiments. R.C. designed and G.G. performed the indirect calorimetry experiments. E.F., L.M., C.Q., and D.P. performed histological analysis. C.H. performed bioinformatics analyses, M.R. performed experiments on cells. S.R., E.F., and L.M. expanded and completed the study. S.B., N.V., and F.G. provided clinical samples. J.P.L., F.R., F.J.S., R.C., E.F., L.M., and S.T.N. designed the experiments and critically revised the manuscript. A.F. and C.V. designed the study and wrote the paper.

DECLARATION OF INTERESTS

The authors declare that they have no conflict of interest.

Received: October 22, 2019
Revised: March 13, 2020
Accepted: April 15, 2020
Published: May 22, 2020

REFERENCES

Anderson, D.M., Makarewich, C.A., Anderson, K.M., Shelton, J.M., Bezprozvannaya, S., Bassel-Duby, R., and Olson, E.N. (2016). Widespread control of calcium signaling by a family of SERCA-inhibiting micropeptides. Sci. Signal. *9*, ra119.

Babu, G.J., Bhupathy, P., Carnes, C.A., Billman, G.E., and Periasamy, M. (2007). Differential expression of sarcolipin protein during muscle development and cardiac pathophysiology. J. Mol. Cell. Cardiol. *43*, 215–222.

Bal, N.C., Maurya, S.K., Sopariwala, D.H., Sahoo, S.K., Gupta, S.C., Shaikh, S.A., Pant, M., Rowland, L.A., Goonasekera, S.A., Molkentin, J.D., et al. (2012). Sarcolipin is a newly identified regulator of muscle-based thermogenesis in mammals. Nat. Med. *18*, 1575–1579.

Batran, R. Al, Gopal, K., Aburasayn, H., Eshreif, A., Almutairi, M., Greenwell, A.A., Campbell, S.A., Saleme, B., Court, E.A., Eaton, F., et al. (2019). The antianginal ranolazine mitigates obesity-induced nonalcoholic fatty liver disease and increases hepatic pyruvate dehydrogenase activity. JCI Insight *4*, e124643.

Belardinelli, Liu, Smith-Maxwell, Wang, El-Bizri, Hirakawa, Karpinski, Li, Hu, Li, Crumb, Wu, Koltun, Zablocki, Yao, Dhalla, Rajamani, and Shryock. (2013). J. Pharmacol. Exp Ther. https://doi.org/10.1124/jpet.112.198887.

Bhandari, B., and Subramanian, L. (2007). Ranolazine, a partial fatty acid oxidation inhibitor, its potential benefit in angina and other cardiovascular disorders. Recent Pat. Cardiovasc. Drug Discov. *2*, 35–39.

Bouteloup, C., Desport, J.-C., Clavelou, P., Guy, N., Derumeaux-Burel, H., Ferrier, A., and Couratier, P. (2009). Hypermetabolism in ALS patients: an early and persistent phenomenon. J. Neurol. *256*, 1236–1242.

Calvo, A.C., Manzano, R., Atencia-Cibreiro, G., Oliván, S., Muñoz, M.J., Zaragoza, P., Cordero-Vázquez, P., Esteban-Pérez, J., García-Redondo, A., and Osta, R. (2012). Genetic biomarkers for ALS disease in transgenic SOD1(G93A) mice. PLoS One *7*, e32632.

Capitanio, D., Vasso, M., Ratti, A., Grignaschi, G., Volta, M., Moriggi, M., Daleno, C., Bendotti, C., Silani, V., and Gelfi, C. (2012). Molecular signatures of amyotrophic lateral sclerosis disease progression in hind and forelimb muscles of an SOD1G93A mouse model. Antioxid. Redox Signal. *17*, 1333–1350.

Desport, J.-C., Torny, F., Lacoste, M., Preux, P.-M., and Couratier, P. (2005). Hypermetabolism in ALS: correlations with clinical and paraclinical parameters. Neurodegener. Dis. *2*, 202–207.

Dobrowolny, G., Aucello, M., Rizzuto, E., Beccafico, S., Mammucari, C., Boncompagni, S., Bonconpagni, S., Belia, S., Wannenes, F., Nicoletti, C., et al. (2008). Skeletal muscle is a primary target of SOD1G93A-mediated toxicity. Cell Metab. *8*, 425–436.

Dobrowolny, G., Lepore, E., Martini, M., Barberi, L., Nunn, A., Scicchitano, B.M., and Musarò, A. (2018). Metabolic changes associated with muscle expression of SOD1 (G93A). Front. Physiol. *9*, 831.

Doshi, S., Gupta, P., and Kalb, R.G. (2017). Genetic induction of hypometabolism by ablation of MC4R does not suppress ALS-like phenotypes in the G93A mutant SOD1 mouse model. Sci. Rep. *7*, 13150.

Dupuis, L., Corcia, P., Fergani, A., Gonzalez De Aguilar, J.L., Bonnefont-Rousselot, D., Bittar, R., Seilhean, D., Hauw, J.J., Lacomblez, L., Loeffler, J.P., et al. (2008). Dyslipidemia is a protective factor in amyotrophic lateral sclerosis symbol. Neurology *70*, 1004–1009.

Fajardo, V.A., Rietze, B.A., Chambers, P.J., Bellissimo, C., Bombardier, E., Quadrilatero, J., and Tupling, A.R. (2017). Effects of sarcolipin deletion on skeletal muscle adaptive responses to functional overload and unload. Am. J. Physiol. Cell Physiol. *313*, C154–C161.

Flück, M. (2006). Functional, structural and molecular plasticity of mammalian skeletal muscle in response to exercise stimuli. J. Exp. Biol. *209*, 2239–2248.

Funalot, B., Desport, J.-C., Sturtz, F., Camu, W., and Couratier, P. (2009). High metabolic level in patients with familial amyotrophic lateral sclerosis. Amyotroph. Lateral Scler. *10*, 113–117.

Genin, E.C., Madji Hounoum, B., Bannwarth, S., Fragaki, K., Lacas-Gervais, S., Mauri-Crouzet, A., Lespinasse, F., Neveu, J., Ropert, B., Augé, G., et al. (2019). Mitochondrial defect in muscle precedes neuromuscular junction degeneration and motor neuron death in CHCHD10 S59L/+ mouse. Acta Neuropathol. *138*, 123–145.

Ghiasi, P., Hosseinkhani, S., Noori, A., Nafissi, S., and Khajeh, K. (2012). Mitochondrial complex I deficiency and ATP/ADP ratio in lymphocytes of amyotrophic lateral sclerosis patients. Neurol. Res. *34*, 297–303.

Goode, J.M., Pearen, M.A., Tuong, Z.K., Wang, S.C.M., Oh, T.G., Shao, E.X., and Muscat, G.E.O. (2016). The nuclear receptor, Nor-1, induces the physiological responses associated with exercise. Mol. Endocrinol. *30*, 660–676.

Granata, C., Jamnick, N.A., and Bishop, D.J. (2018). Training-induced changes in mitochondrial content and respiratory function in human skeletal muscle. Sports Med. *48*, 1809–1828.

Hardie, D.G., Schaffer, B.E., and Brunet, A. (2016). AMPK: an energy-sensing pathway with multiple inputs and outputs. Trends Cell Biol. *26*, 190–201.

Hegedus, J., Putman, C.T., Tyreman, N., and Gordon, T. (2008). Preferential motor unit loss in the SOD1 G93A transgenic mouse model of amyotrophic lateral sclerosis. J. Physiol. *586*, 3337–3351.

Hood, D.A. (2009). Mechanisms of exercise-induced mitochondrial biogenesis in skeletal muscle. Appl. Physiol. Nutr. Metab. *34*, 465–472.

Hu, R., Yan, H., Fei, X., Liu, H., and Wu, J. (2017). Modulation of glucose metabolism by a natural compound from Chloranthus japonicus via activation of AMP-activated protein kinase. Sci. Rep. *7*, 778.

Hunter, R.W., Hughey, C.C., Lantier, L., Sundelin, E.I., Peggie, M., Zeqiraj, E., Sicheri, F., Jessen, N., Wasserman, D.H., and Sakamoto, K. (2018). Metformin reduces liver glucose production by inhibition of fructose-1-6-bisphosphatase. Nat. Med. *24*, 1395–1406.

Ioannides, Z.A., Ngo, T., and Henderson, D. (2016). Altered metabolic homeostasis in amyotrophic lateral sclerosis: mechanisms of energy imbalance and contribution to disease progression. Neurodegener. Dis. *16*, 382–397.

Jésus, P., Fayemendy, P., Nicol, M., Lautrette, G., Sourisseau, H., Preux, P.-M., Desport, J.-C., Marin, B., and Couratier, P. (2018). Hypermetabolism is a deleterious prognostic factor in patients with amyotrophic lateral sclerosis. Eur. J. Neurol. *25*, 97–104.

Kasarskis, E.J., Mendiondo, M.S., Matthews, D.E., Mitsumoto, H., Tandan, R., Simmons, Z., Bromberg, M.B., and Kryscio, R.J. (2014). Estimating daily energy expenditure in individuals with amyotrophic lateral sclerosis. Am. J. Clin. Nutr. *99*, 792–803.

Leonard, S., Tobin, L.M., and Findlay, J.B.C. (2017). The signalling mechanisms of a novel mitochondrial complex I inhibitor prevent lipid accumulation and attenuate TNF-α-induced insulin resistance in vitro. Eur. J. Pharmacol. *800*, 1–8.

Lundsgaard, A.-M., Fritzen, A.M., and Kiens, B. (2018). Molecular regulation of fatty acid oxidation in skeletal muscle during aerobic exercise. Trends Endocrinol. Metab. *29*, 18–30.

Maurya, S.K., and Periasamy, M. (2015). Sarcolipin is a novel regulator of muscle metabolism and obesity. Pharmacol. Res. *102*, 270–275.

Maurya, S.K., Herrera, J.L., Sahoo, S.K., Reis, F.C.G., Vega, R.B., Kelly, D.P., and Periasamy, M. (2018). Sarcolipin signaling promotes mitochondrial biogenesis and oxidative metabolism in skeletal muscle. Cell Rep. *24*, 2919–2931.

McCormack, J.G., Stanley, W.C., and Wolff, A.A. (1998). Ranolazine: a novel metabolic modulator for the treatment of angina. Gen. Pharmacol. *30*, 639–645.

Mejzini, R., Flynn, L.L., Pitout, I.L., Fletcher, S., Wilton, S.D., and Akkari, P.A. (2019). ALS genetics, mechanisms, and therapeutics: where are we now? Front. Neurosci. *13*, 1310.

Merrill, G.F., Kurth, E.J., Hardie, D.G., and Winder, W.W. (1997). AICA riboside increases AMP-activated protein kinase, fatty acid oxidation, and glucose uptake in rat muscle. Am. J. Physiol. Endocrinol. Metab. *273*, E1107–E1112.

Moglia, C., Calvo, A., Grassano, M., Canosa, A., Manera, U., D'ovidio, F., Bombaci, A., Bersano, E., Mazzini, L., Mora, G., et al. (2019). Early weight loss in amyotrophic lateral sclerosis: outcome relevance and clinical correlates in a population-based cohort. J. Neurol. Neurosurg. Psychiatry *90*, 666–673.

Ning, Y., Zhen, W., Fu, Z., Jiang, J., Liu, D., Belardinelli, L., and Dhalla, A.K. (2011). Ranolazine increases β-cell survival and improves glucose homeostasis in low-dose streptozotocin-induced diabetes in mice. J. Pharmacol. Exp. Ther. *337*, 50–58.

O'Neill, H.M., Holloway, G.P., and Steinberg, G.R. (2013). AMPK regulation of fatty acid metabolism and mitochondrial biogenesis: implications for obesity. Mol. Cell. Endocrinol. *366*, 135–151.

Palamiuc, L., Schlagowski, A., Ngo, S.T., Vernay, A., Dirrig-Grosch, S., Henriques, A., Boutillier, A.-L., Zoll, J., Echaniz-Laguna, A., Loeffler, J.-P., et al. (2015). A metabolic switch toward lipid use in glycolytic muscle is an early pathologic event in a mouse model of amyotrophic lateral sclerosis. EMBO Mol. Med. *7*, 526–546.

Patel, V.D., and Hasumati, R. (2015). Ranolazine: a review on analytical method and its determination in synthetic mixture. Asian J. Pharm. Anal. *5*, 214.

Pearen, M.A., Goode, J.M., Fitzsimmons, R.L., Eriksson, N.A., Thomas, G.P., Cowin, G.J., Mary Wang, S.C., Tuong, Z.K., and Muscat, G.E.O. (2013). Transgenic muscle-specific Nor-1 expression regulates multiple pathways that effect adiposity, metabolism, and endurance. Mol. Endocrinol. *27*, 1897–1917.

Peggion, C., Massimino, M.L., Biancotto, G., Angeletti, R., Reggiani, C., Sorgato, M.C., Bertoli, A., Stella, R., and Stella, R. (2017). Absolute quantification of myosin heavy chain isoforms by selected reaction monitoring can underscore skeletal muscle changes in a mouse model of amyotrophic lateral sclerosis. Anal. Bioanal. Chem. *409*, 2143–2153.

Quijano, C., Trujillo, M., Castro, L., and Trostchansky, A. (2016). Interplay between oxidant species and energy metabolism. Redox Biol. *8*, 28–42.

Rosca, M.G., Vazquez, E.J., Chen, Q., Kerner, J., Kern, T.S., and Hoppel, C.L. (2012). Oxidation of fatty acids is the source of increased mitochondrial reactive oxygen species production in kidney cortical tubules in early diabetes. Diabetes *61*, 2074–2083.

Rossi, S., Serrano, A., Gerbino, V., Giorgi, A., Di Francesco, L., Nencini, M., Bozzo, F., Schininà, M.E., Bagni, C., Cestra, G., et al. (2015). Nuclear accumulation of mRNAs underlies G4C2-repeat-induced translational repression in a cellular model of C9orf72 ALS. J. Cell Sci. *128*, 1787–1799.

Salvatori, I., Valle, C., Ferri, A., and Carrì, M.T. (2017). SIRT3 and mitochondrial metabolism in neurodegenerative diseases. Neurochem. Int. *109*, 184–192.

Salvatori, I., Ferri, A., Scaricamazza, S., Giovannelli, I., Serrano, A., Rossi, S., D'Ambrosi, N., Cozzolino, M., Di Giulio, A., Moreno, S., et al. (2018). Differential toxicity of TAR DNA-binding protein 43 isoforms depends on their submitochondrial localization in neuronal cells. J. Neurochem. *146*, 585–597.

Smith, W.S., Broadbridge, R., East, J.M., and Lee, A.G. (2002). Sarcolipin uncouples hydrolysis of ATP from accumulation of Ca2+ by the Ca2+-ATPase of skeletal-muscle sarcoplasmic reticulum. Biochem. J. *361*, 277–286.

Stanley, W.C. (2002). Partial fatty acid oxidation inhibitors for stable angina. Expert Opin. Investig. Drugs *11*, 615–629.

Steyn, F.J., Ioannides, Z.A., Van Eijk, R.P.A., Heggie, S., Thorpe, K.A., Ceslis, A., Heshmat, S., Henders, A.K., Wray, N.R., Van Den Berg, L.H., et al. (2018). Hypermetabolism in ALS is associated with greater functional decline and shorter survival. J. Neurol. Neurosurg. Psychiatry *89*, 1016–1023.

Thomas, H.E., Zhang, Y., Stefely, J.A., Veiga, S.R., Thomas, G., Kozma, S.C., and Mercer, C.A. (2018). Mitochondrial complex I activity is required for maximal autophagy. Cell Rep. *24*, 2404–2417.e8.

Tintignac, L.A., Brenner, H.R., and Rüegg, M.A. (2015). Mechanisms regulating neuromuscular

junction development and function and causes of muscle wasting. Physiol. Rev. *95*, 809–852.

Tsitkanou, S., Gatta, P.A.D., and Russell, A.P. (2016). Skeletal muscle satellite cells, mitochondria, and MicroRNAs: their involvement in the pathogenesis of ALS. Front. Physiol. *7*, 403.

Wang, W., Wang, L., Lu, J., Siedlak, S.L., Fujioka, H., Liang, J., Jiang, S., Ma, X., Jiang, Z., Da Rocha, E.L., et al. (2016). The inhibition of TDP-43 mitochondrial localization blocks its neuronal toxicity. Nat. Med. *22*, 869–878.

Widmann, M., Nieß, A.M., and Munz, B. (2019). Physical exercise and epigenetic modifications in skeletal muscle. Sports Med. *49*, 509–523.

Wiedemann, F.R., Winkler, K., Kuznetsov, A.V., Bartels, C., Vielhaber, S., Feistner, H., and Kunz, W.S. (1998). Impairment of mitochondrial function in skeletal muscle of patients with amyotrophic lateral sclerosis. J. Neurol. Sci. *156*, 65–72.

Yin, H., Price, F., and Rudnicki, M.A. (2013). Satellite cells and the muscle stem cell niche. Physiol. Rev. *93*, 23–67.

Zurlo, F., Larson, K., Bogardus, C., and Ravussin, E. (1990). Skeletal muscle metabolism is a major determinant of resting energy expenditure. J. Clin. Invest. *86*, 1423–1427.

iScience, Volume *23*

Supplemental Information

Skeletal-Muscle Metabolic Reprogramming in ALS-SOD1^{G93A} Mice Predates Disease Onset and Is A Promising Therapeutic Target

Silvia Scaricamazza, Illari Salvatori, Giacomo Giacovazzo, Jean Philippe Loeffler, Frederique Renè, Marco Rosina, Cyril Quessada, Daisy Proietti, Constantin Heil, Simona Rossi, Stefania Battistini, Fabio Giannini, Nila Volpi, Frederik J. Steyn, Shyuan T. Ngo, Elisabetta Ferraro, Luca Madaro, Roberto Coccurello, Cristiana Valle, and Alberto Ferri

Figure S1

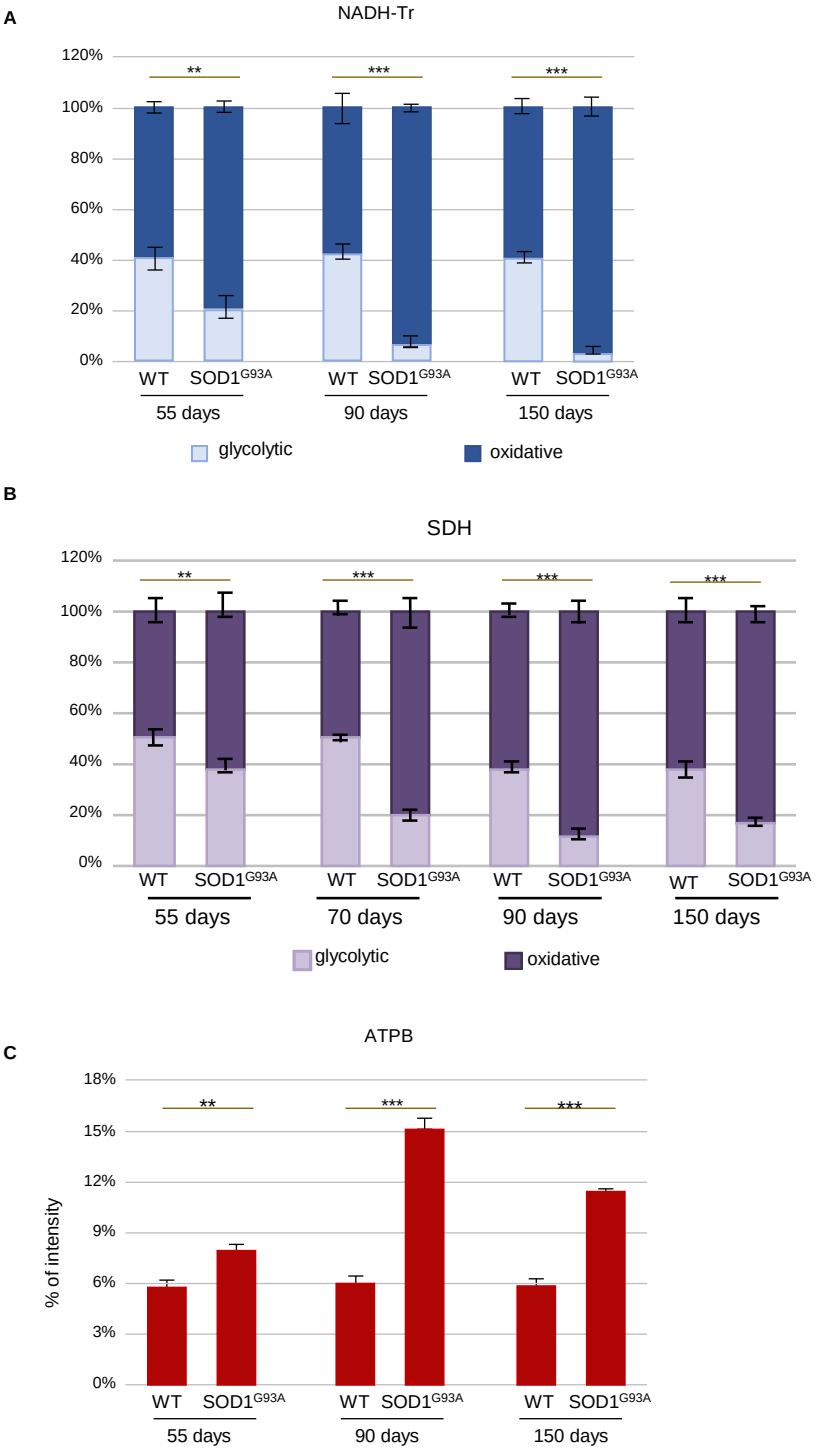

Figure S1. Quantification of muscle oxidative markers, Related to Figure 2. (A-B) Percentages of the dark areas (Blue for NADH-Tr activity and Purple for SDH activity, respectively) measured using ImageJ and normalized against total area. **(C)** Percentages of the red areas (ATBP fluorescent signal) measured using ImageJ and normalized against total area. Calculations were performed on tibialis anterior (TA) cryosections (3 for each mouse) from 3 to 4 different mice at each age. Data presented as means ± SEM, ***P*<0,001, ****P*<0,0001 with respect to wild-type control littermates at the same age, unpaired Student's *t* tes.

Figure S2

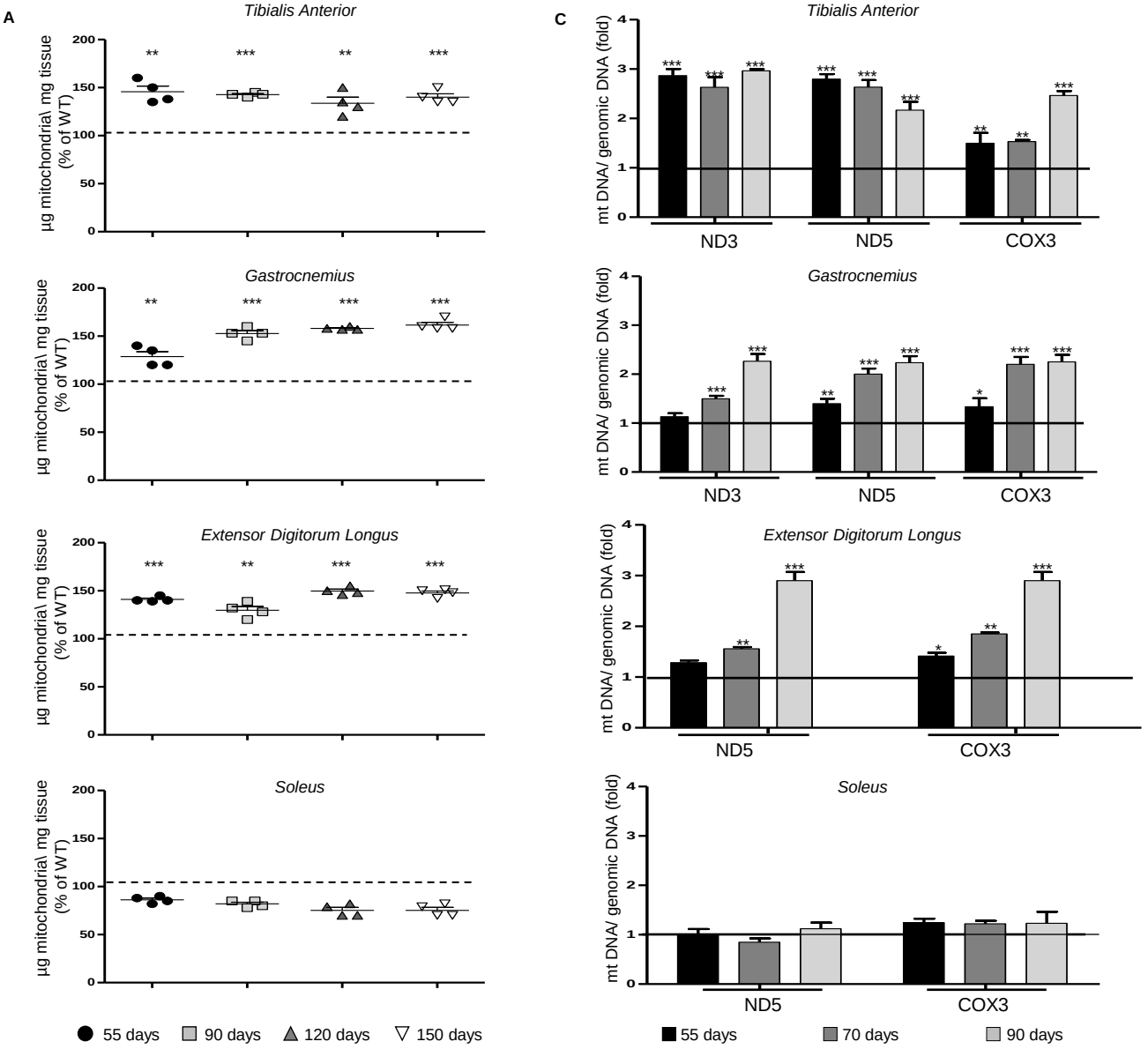

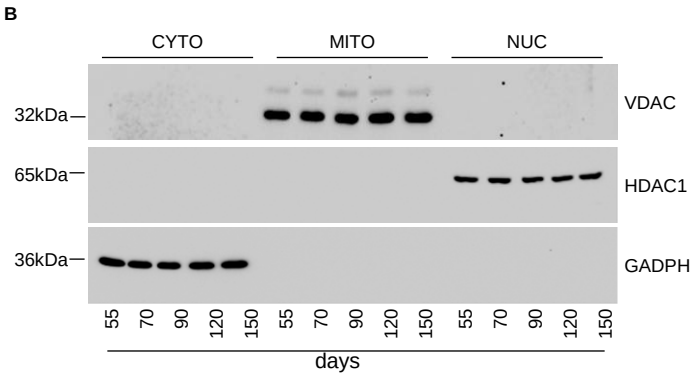

Figure S2. The mass of mitochondria increases during disease course, Related to Figure 2. Mitochondrial amount was determined at 55, 90, 120 and 150 days of age by assessing: **(A)** The ratio between ug of purified mitochondria and mg of tissue used for purification; *tibialis anterior* (TA), *gastrocnemius* (GNM), *extensor digitorum longus* (EDL) and *soleus.* Data are reported as percentage, with 100% being assigned to values obtained from age-matched wild-type control mice (WT), $n = 4$ independent experiments. **(B)** Western blot analysis of cytosolic (CYTO), mitochondrial (MITO) and nuclear (NUC) subcellular fractions obtained from the TA of WT mice from 55 to 150 days of age. Fractions were verified for the presence of specific markers using antibodies against GADPH for the cytosolic fraction, VDAC for the mitochondrial fraction and HDAC1 for the nuclear fraction. A representative immunoblot is shown. **(C)** RT-qPCR quantification of ND3, ND5 and COX3 genes encoded by mitochondrial DNA in the TA, GNM, EDL and soleus muscle. Genomic DNA was used as internal standard and values of age-matched wild-type control mice was arbitrary set at 1. Data are presented as mean ± SEM, *P<0,05, **P<0,001, ***P<0,0001, unpaired Student's t test, n=4 different mice for each age.

Figure S3

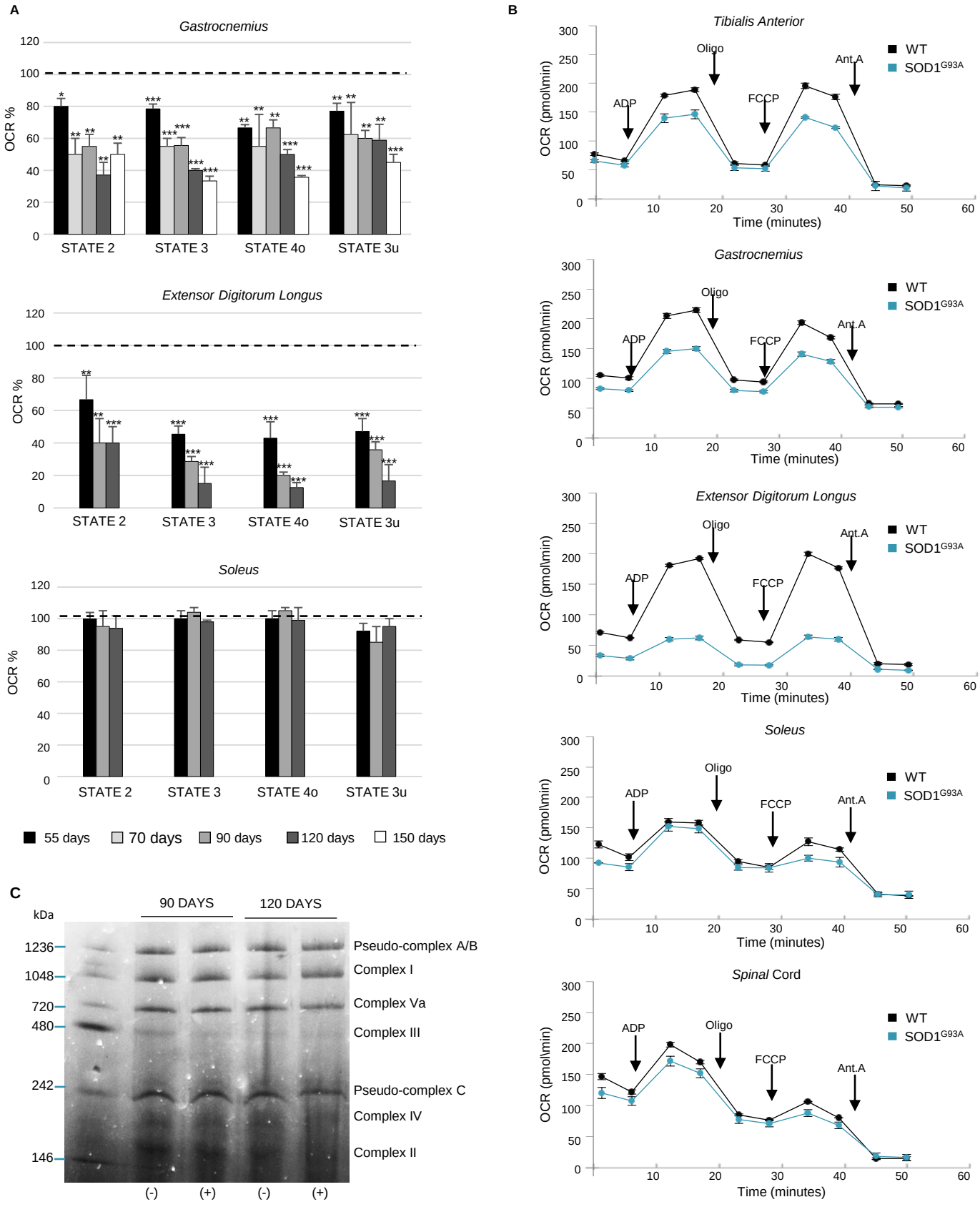

Figure S3. Mitochondrial bioenergetic failure occurs in skeletal muscle of early presymptomatic SOD1 G93A mice, Related to Figure 3. (A) Coupling assay on isolated mitochondria purified from different tissues of SOD1^{G93A} mice at the indicated ages. Mitochondrial respiration stages are reported: basal respiration (State 2), maximally coupled respiration (State 3), respiration due to proton leak (State 4o) and maximal uncoupled respiration (State 3u). Data are expressed as % of Oxygen Consumption Rate (OCR) and 100% was arbitrarily assigned to values obtained from age-matched wild-type mice. *P<0,05, **P<0,001, ***P<0,0001, unpaired Student's t test. **(B)** Representative Coupling Assay profiles performed on mitochondria isolated from the indicated tissues of 55 day old SOD1^{G93A}mice and their wild-type control littermates. The injection of ADP, Oligomycin, FCCP and Antimycin A (Ant. A) are indicated with arrows. **(C)** Blue Native Gel mitochondrial extracts isolated from the TA of WT (-) and SOD1^{G93A} (+) mice at the indicated ages. A representative gel is shown (n=3 experiments).

Figure S4

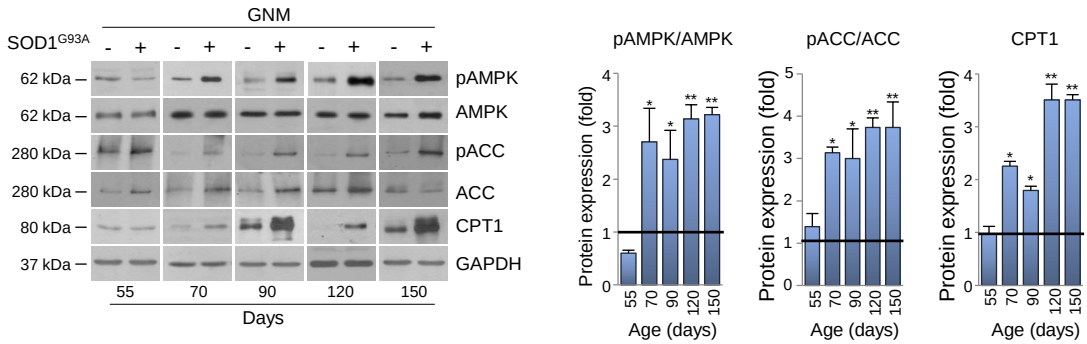

Figure S4. Alterations in metabolic targets occur early in the *gastrocnemius* of SOD1^{G93A} mice, Related to Figure 5. Western blot analysis of pAMPK, AMPK, pACC, ACC and CPT1 in the *gastrocnemius* (GMN) of SOD1^{G93A} (+) and wild type mice (-) from 55 days of age to end-stage (150 days) of disease. GAPDH was used as loading control (left panel). Densitometric analysis of pAMPK/AMPK and pACC/ACC ratios, and CPT1 expression (right panel). Data are presented as mean ± SEM, **P*<0,05, ***P*<0,001 when compared with wild-type mice at the same age (arbitrarily set at 1), *n* = 4 independent experiments, unpaired Student's *t* test.

Figure S5

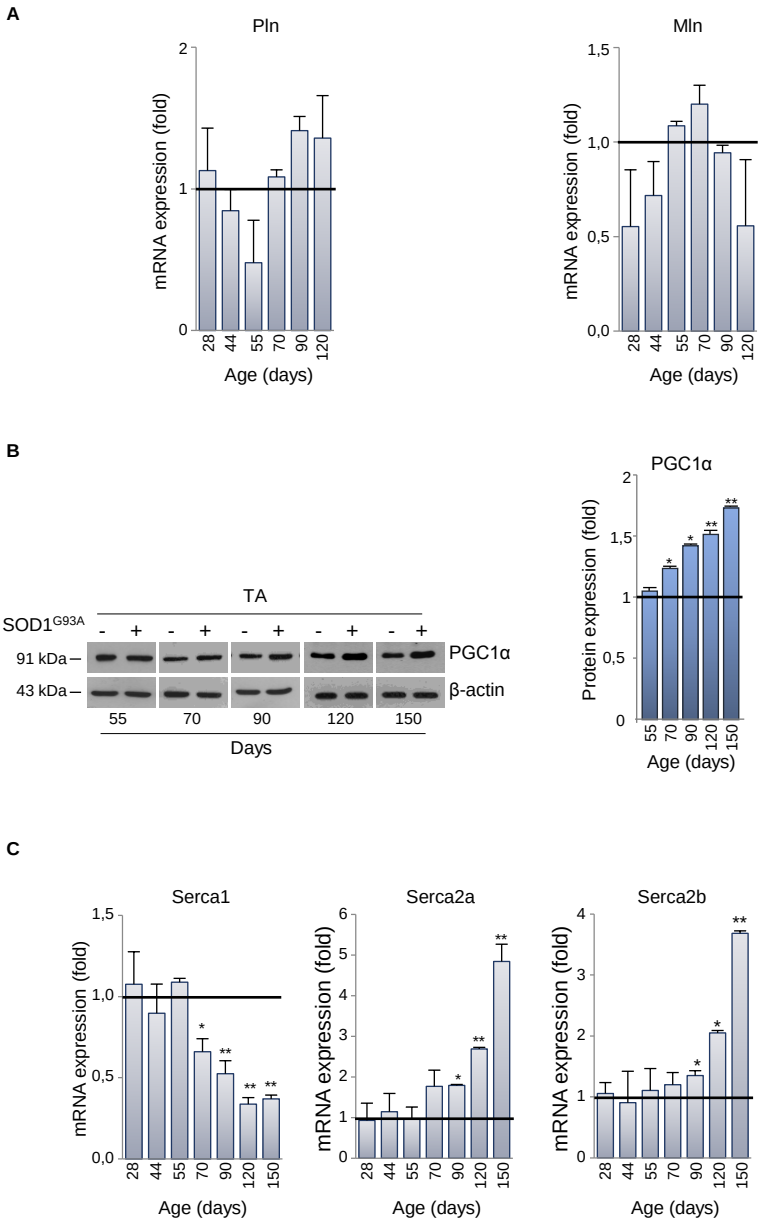

Figure S5. Expression of other SERCA regulating micropeptides, Related to Figure 6. (A) Expression of mRNAs coding for phospholamban (PLN) and myoregulin (MLN) in *tibialis anterior* of SOD1^{G93A} mice. RT-qPCR analysis was performed at different stages of disease in SOD1^{G93A} mice and their wild-type control littermates. **(B)** PGC1α expression in skeletal muscle of SOD1^{G93A} mice. PGC1α protein expression in *tibialis anterior* (TA) of SOD1^{G93A} (+) and wild type mice (-) at the indicated ages (left panel). β-Actin was used as loading control. Densitometric analysis of data (right panel), presented as mean ± SEM, **P*<0,05, ***P*<0,001, when compared with wild-type mice at the same age (arbitrarily set ~~on~~ at 1), *n* = 4 independent experiments, unpaired Student's *t* test. **(C)** Expression of mRNAs coding for Serca1, Serca2a, Serca2b in the TA of SOD1^{G93A} mice. RT-qPCR analysis was performed at different stages of disease in SOD1^{G93A} mice and their wild-type control littermates (at least *n*=3 for each stage). Results in **A** and **C** (at least *n*=3 for each stage) are expressed as the ratio between the average of values from wild-type control and transgenic mice, normalized to the average values of TATA box housekeeping gene. Data are presented as mean ± SEM when compared with control littermates at the same age (arbitrarily set ~~on~~ at 1), unpaired Student's *t* test.

Figure S6

A

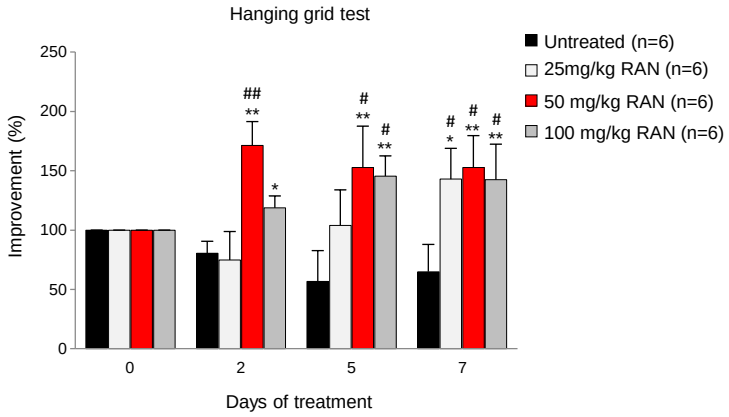

B

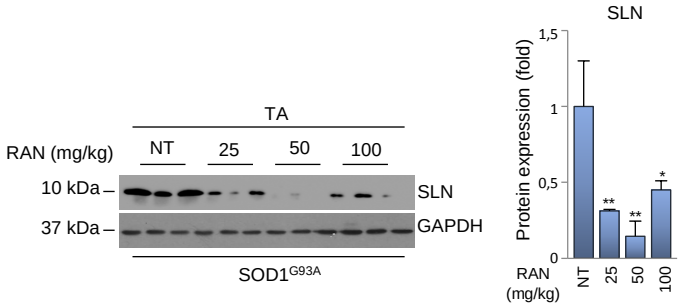

Figure S6. Dose response study of Ranolazine treatment, Related to Figure 7. (A) Locomotor abilities of SOD1^{G93A} mice receiving daily intraperitoneal injection of different doses of Ranolazine (RAN) (25, 50 and 100 mg/kg) or physiological solution (untreated) for seven days (from 110 to 117 days of age) evaluated by hanging grid test at the indicated days. Performance at day 0 of treatment was considered as 100% and performance, at days 2, 5 and 7, were considered relative to time 0. *P<0,05, **P<0,001 when compared with untreated SOD1^{G93A} and $^{\#}P$<0,05, $^{\#\#}P$<0,001 when compared with SOD1^{G93A} performance at the beginning of treatment. **(B)** Western blot analysis of Sarcolipin (SLN) in the *tibialis anterior* (TA) of SOD1^{G93A} receiving daily intraperitoneal injection of RAN 25 mg/kg (25), 50 mg/kg (50), 100 mg/kg (100) or physiological solution (NT) for seven days (left panel). GAPDH antibody was used as loading control. Densitometric analysis of data (right panel). *P<0,05, **P<0,001 when compared with untreated mice (arbitrarily set at 1). Data are presented as mean ± SEM of $n = 6$ independent experiments, parametric two-way ANOVA with Bonferroni *post hoc* test (A) and one-way ANOVA with Bonferroni *post hoc* test (A).

Figure S7

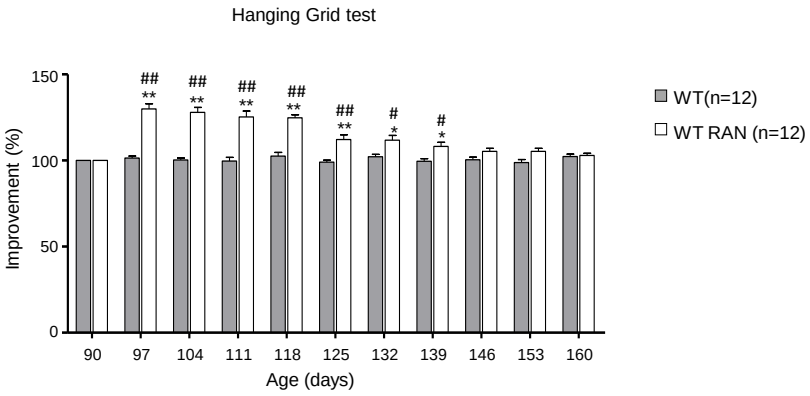

Figure S7. Ranolazine (RAN) treatment effect in wild-type (WT) mice, Related to Figure 7. Locomotor abilities of WT mice receiving daily intraperitoneal injection of Ranolazine 50 mg/kg (WT RAN) or physiological solution (WT) evaluated by hanging grid test at the indicated days. Performance was evaluated from 90 days of age (start of treatment) to an age that equates to the end-stage of disease for $SOD1^{G93A}$ mice. Data are presented as mean ± SEM, **P*<0,05 ***P*<0,001 when compared with age-matched WT untreated mice and $^{\#}P$<0,05 $^{\#\#}P$<0,01 when compared with WT mice at the beginning of treatment, *n*=11 WT, *n* = 11 WT RAN, parametric two-way ANOVA with Bonferroni *post hoc* test.

METHODS

Antibodies

The antibodies used in this study were: AMPKα rabbit polyclonal (Cell Signaling, Cat#2532 WB:1:1000), Phospho-AMPKα (Thr172) (40H9) rabbit monoclonal (Cell Signaling, Cat#2535 WB:1:1000), Acetyl-CoA Carboxylase (c83b10) rabbit monoclonal (Cell Signaling, Cat#3676 WB:1:1000), Phospho-Acetyl-CoA Carboxylase (Ser79) rabbit polyclonal (Cell Signaling, Cat#3661 WB:1:1000), anti-CPT1A (8F6AE9) mouse monoclonal (Abcam 128568 WB:1:1000), anti-Sarcolipin rabbit polyclonal (Millipore Cat#ABT13 WB 1:1000), CaMKIIα (A-1) mouse monoclonal (Santa Cruz Biotechnology Inc,. Cat# sc-13141 WB 1:1000), Phospho-CaMKIIα (22B1) mouse monoclonal (Santa Cruz Biotechnology Inc., Cat# sc-32289 WB 1:1000), PGC1alpha (H-300) Rabbit polyclonal (Santa Cruz Biotechnology Inc., Cat# sc-13067 WB 1:1000), anti-Laminin rabbit polyclonal (Cat#L9393, Sigma, IF 1:400), Anti- ATPB (3D5) mouse monoclonal (Abcam Cat#ab14730 IF 1:400), anti-HDAC1 rabbit polyclonal (Santa Cruz Biotechnology Inc., Cat# sc-7872, RRID:AB_2279709, WB 1 : 1000), anti-VDAC mouse monoclonal (Santa Cruz Biotechnology Inc., Cat# sc-8829, RRID:AB_2214801, WB 1 : 5000), anti-GAPDH mouse monoclonal (Santa Cruz Biotechnology Inc., Cat# sc-166545, RRID:AB_2107299 WB 1:5000), anti-β-Actin (Santa Cruz Biotechnology Inc., Cat# sc-47778, WB 1:5000). Anti-rabbit (Cat# 1706515, WB: 1:1000) and anti-mouse (Cat# 1706516, WB: 1:1000) IgG peroxidase-conjugated secondary antibodies were from Bio-Rad Laboratories, Hercules, CA, USA and Alexa Fluor 488 (Invitrogen, Cat# A11017, 1: 300) anti-rabbit goat antibodies and Cy3 anti-mouse antibody from Jackson Immuno-Research Laboratories, West Grove, PA, USA, Cat# 65119, 1: 300).

Animals

All animal procedures were carried out in accordance with the European Guidelines for the use of animals in research (2010/63/EU) and the requirements of Italian laws (D.L. 26/2014). All procedures were approved by the Animal welfare office, Department of Public Health and Veterinary, Nutrition and Food Safety, General Management of Animal Care and Veterinary Drugs of the Italian Ministry of Health (protocol number 931/2017/PR). Animals were kept in a virus/antigen-free facility with a light/dark cycle of 12 h at constant temperature and humidity. Food and water were provided *ad libitum*.

SOD1^{G93A} mice (B6.Cg-Tg(SOD1 G93A)1Gur/J) were obtained from The Jackson Laboratory (Bar Harbor, ME, USA) and bred in our animal facility. Transgenic hemizygous SOD1^{G93A} males were crossbred with C57BL/6 females and transgenic progeny were genotyped by PCR. Disease onset was evaluated by hanging grid test; tests were conducted once per week starting at 55 days of age. The final measurement for each mouse was determined by calculating the mean of three different hanging grid test trials on each given day. A performance baseline of 100% was assigned to the first mean performance for each mouse at 55 days of age. Age of symptom onset was classified as being the time at which mouse performance deteriorated by 20% from the baseline. In our animal house, and using this approach, disease onset in male mice was classified as being 91.7 ± 2.9 days, and survival was 168.7 ± 1.9 days.

To follow disease progression, behavioural scores and body weight were monitored starting at 55 days according to Apolloni et al. (Apolloni et al., 2019). In brief, we assigned the following age (in days) to the following disease stages: 55 days as “early presymptomatic”, 70 days as “presymptomatic”, 90 days as “symptoms onset”, 120 days as “symptomatic”, 150 days as “end stage”. Mice were anaesthetized with Rompum (xylazine, 20 mg/ml, 0.5 ml/kg Bayer, Milan, Italy) plus Zoletil (tiletamine and zolazepam, 100 mg/ml, 0.5 ml/kg; Virbac, Milan, Italy), and then sacrificed for tissue dissection.

Energy metabolism by indirect calorimetry

Total Energy Expenditure (EE), Resting Energy Expenditure (REE) and Respiratory Exchange Ratio (RER) were measured using an indirect calorimeter system (TSE PhenoMaster/LabMaster System, Germany) with a constant air flow of 0.35 L/min. Mice were adapted for 12 hours to the metabolic chamber, and parameters were measured at 20 minute intervals for each mouse, starting at 7:00 PM and ending automatically after 48h or 72h (12h dark-light phase comparison). Room temperature was kept constant (22˚±1˚C) and locomotor activity was assessed in parallel to discriminate between EE and REE. REE was analyzed by considering each animal's resting conditions, which was defined as an activity count between 0 and 3. RER was calculated as: RER = volume of CO_2 produced/volume of O_2 consumed (an index of substrate utilization). Mice were assessed under standard nutritional conditions (i.e., standard diet-fed) and food intake was continuously monitored (Giacovazzo et al., 2018)**.**

Glucose tolerance test (GTT)

GTT was performed in SOD1^{G93A} and WT mice at 55 days, 90 days and 120 days of age. Blood glucose was measured in tail tip blood samples using a Multicare Test Strip apparatus (Biochemical Systems International, Italy). Plasma glucose was assessed at 0, 20', 40' and 60 min after i.p. glucose administration (2gr/kg), which was administered following an overnight fast (16h). The area under the curve was calculated using the trapezoidal rule.

RNAseq

Total RNA from the *tibialis anterior* (TA) muscles of 90 day old SOD1^{G93A} mice and their wild-type control littermates was extracted using TRI Reagent (Sigma) following the manufacturer's protocol. RNA was shipped to the sequencing IGA of Udine (https://appliedgenomics.org/it/). The libraries for sequencing were prepared using NuGEN Ovation System V2 RNA–Seq. For each biological sample two independent experiments were carried out for the isolation of RNA.

Read quality control was asserted through FastQC (https://www.bioinformatics.babraham.ac.uk/projects/fastqc/), and quality/adapter trimming was carried out using Trim Galore (https://www.bioinformatics.babraham.ac.uk/projects/trim_galore/), which itself is a wrapper for cutadapt. Subsequently, reads were pseudo aligned to transcriptome GRCm38 (mm10) using Kallisto version 0.43.1. Count tables were generated in R using the package tximport together with DESeq2. Differential expression of genes was conducted using DESeq2 with default options. Genes were considered differentially expressed if the adjusted *P*-value was<0.05.

RNA-seq data of this study have been deposited in the Sequence Read Archive (SRA) under the accession code: PRJNA623256 (https://www.ncbi.nlm.nih.gov/Traces/study/?acc=PRJNA623256)

Histochemistry and Immunofluorescence

For histochemistry and immunofluorescence analysis, 10 µm muscle cryosections were obtained from SOD1^{G93A} mice and their wild-type control littermates at different stages of the disease.

For NADH-tetrazolium reductase activity staining (NADH-TR), muscle cryosections were incubated for 15 min with a solution containing NADH and nitrotetra-zolium blue (# N8129 and #N6876, Sigma-Aldrich) in Tris-HCl (pH 7.4) at 37°C (Madaro et al., 2013). Enzymatic staining for succinate dehydrogenase (SDH) activity was performed according to Molinari et al. (Molinari et al., 2017). Briefly, TA cross-sections were incubated for 20′ at 37 °C in PBS containing 1 mg/ml of nitrotetrazolium blue chloride (Sigma-Aldrich, St. Louis, MO, USA) and 27 mg/ml of Na-succinate. After staining, sections were fixed with 4% PFA and images from three serial sections per animal were acquired using an Olympus BX53 (Olympus). Images were processed using Image analysis IAS software (Delta Sistemi).

For immunofluorescence, cryosections were fixed in 4% PFA for 10 min, permeabilized with 0.25% Triton for 15 min at room temperature, and blocked for 1 h with a solution containing 4% BSA in PBS. Samples were then incubated for 2 h at room temperature with primary antibodies followed by Alexa 488- or Cy5- conjugated secondary antibodies. After rinsing in PBS, cryosections were counterstained with 1 *μ*g/ml Hoechst 33342 (Sigma-Aldrich) in PBS and visualized with a Zeiss LSM 800 Confocal Laser Scanning Microscope. Fluorescence images were processed using ZEN 2.6 (Blue Edition) (Carl Zeiss, Milan, Italy) and Adobe Photoshop software (Adobe, San Jose, CA, USA). Densitometric analyses were performed using ImageJ (U. S. National Institutes of Health, Bethesda, Maryland, USA, https://imagej.nih.gov/ij/, 1997-2016).

Isolation, quantification and bioenergetic analysis of isolated mitochondria

Mitochondria were isolated from the TA, gastrocnemius (GNM), extensor digitorum longus (EDL), soleus and spinal cord of $SOD1^{G93A}$ mice and their wild-type control littermates, at different stages of the disease. According to Salvatori et al., tissues were homogenized in 210 mM mannitol, 70 mM sucrose, 1 mM EDTA and 10 mM HEPES KOH (pH 7.5) through a Glass/Teflon Potter Elvehjem homogenizer (Salvatori et al., 2017, 2018). The total concentration of mitochondria was determined using a Bradford assay (Bio-Rad, Cat# 5000006) and the obtained quantity was normalized to the weight of the starting material to determine μg of mitochondria per mg of tissue. Tissue mitochondrial content was also assayed by quantitative real-time PCR in which the quantity of mitochondrial DNA / genomic DNA was evaluated (see also below in “DNA-RNA isolation and Real Time PCR”).

Isolated mitochondria were resuspended in a minimum volume of Respiration Buffer (250 mM Sucrose, 15 mM KCl, 1 mM EGTA, 5 mM $MgCl_2$, 30 mM K_2HPO_4), loaded (4 μg for skeletal muscles and 12 μg for spinal cord) onto a Seahorse XFe96 microplate, and centrifuged for 20 minutes at 2000 x g. After centrifugation 180 μl of Respiration Buffer [containing substrates: pyruvate (5 mM), malate (2.5 mM), glutamate (5 mM)] were added to each well, and the microplate was incubated at 37°C for 8 min to equilibrate the plate temperature. During plate incubation, the XFe96 cartridge was loaded with drugs to a final concentration of: ADP 1 mM, oligomycin 3 μM , FCCP 12 μM and Antimycin A 2 μM. Microplates containing mitochondria were then loaded into Seahorse XFe96 Extracellular Flux Analyzer (Seahorse Bioscience-Agilent) and the assay was completed according to the protocol developed by Seahorse Agilent. Coupling assays were performed across 6 technical replicates per plate, for 3 experiments. This assay allows for the assessment of electron transport chain functionality and oxidative phosphorylation flow tracing O_2 Consumption Rates (OCR) in basal conditions (mitochondrial State 2 respiration) and in response to the administration of ADP (maximal coupled respiration, or mitochondrial State 3 respiration), Oligomycin A (respiration due to proton leak, or mitochondrial State 4o

respiration), FCCP (maximal uncoupled respiration, or mitochondrial State 3u respiration) and Antimycin A (inhibition of oxidative respiration).

Blue Native PAGE (BN-PAGE)
BN-PAGE was performed on mitochondria purified from the TA of SOD1^{G93A} mice and their wild-type control littermates using a NativePAGE™ Sample Prep Kit (Invitrogen™, Cat # BN2008). Specifically, 20ug of mitochondrial protein was loaded into 4-16% gradient gels (Bio-Rad), electrophoresed at 150 V for 120 minutes, and stained with 10% acetic acid, 25% isopropanol and Coomassie blue G250. The apparent molecular weight was determined using NativeMark™ Unstained Protein Standard molecular weight markers (Invitrogen™, Cat # LC0725).

Total ATP evaluation
Total ATP concentration was measured in the TA of SOD1^{G93A} mice and their wild-type control littermates using an ATP Colorimetric/Fluorometric Assay Kit (BioVision, Inc., Milpitas, CA). Samples were loaded in 96-well microtiter plates and the fluorometric measurement of tissue ATP concentration was determined at Ex / Em = 535/587 nm using a plate reader (Perkin Elmer 1420 Multilabel Counter Victor3V).

Biochemical assays
The activity of respiratory chain complexes (Complex I, II/III, IV) was evaluated in isolated mitochondria obtained from ALS mice and their wild-type control littermates at different stages of the disease according to Salvatori et al. (Salvatori et al., 2018), with some modifications. Briefly, tissues were sonicated (UP200S Ultrasound Technology, Hielscher, Teltow, Germany, 20% Amplitude, 0.5 cycles for 30 s) and the reduction or oxidation of specific substrates was recorded by spectrophotometric measures. Complex I activity was performed by monitoring the oxidation of NADH at 340 nm at 30°C in a 1 mL quartz cuvette containing 25 mM potassium phosphate pH 7.4, 5 mM $MgCl_2$, 5 mg/mL bovine serum albumin, 1 mg/mL Antimycin A, 65 µM decylubiquinone, 130 µM NADH and 80 µg of total mitochondrial protein. Complex II/III activity was performed by monitoring the reduction of ferricytochrome c at 540 nm in a 1-ml cuvette at 30°C containing 20mM succinate, 0.5 mM EDTA, 2 mM KCN, and 25 µg total mitochondria protein. Complex IV activity was assayed following the oxidation of ferricytochrome c at 540 nm in a 1 ml cuvette at 30°C. Spectrophotometric determination of citrate synthase activity was measured according to Ferri et al. (Ferri et al., 2006) and values were used as standard internal controls.

Bioenergetic analysis of isolated skeletal muscle satellite cells
Skeletal muscle satellite cells were isolated from 55 day old SOD1^{G93A} mice and age-matched wild-type controls through magnetic beads-associated cells sorting according to Reggio et al. (Reggio et al., 2020). Mice were euthanized via cervical dislocation, and hindlimbs were carefully skinned, dissected and placed in HBSS supplemented with 2% BSA and 1% Pen/Strep (SupHBSS). Muscles were dissociated from bones in a sterile hood and minced into small pieces. Minced tissue was separated at 700 x g for 10 min at 4°C and digested with 2 µg/µl collagenase A (Roche), 2.4 U/ml dispase II (Roche), and 10 µg/ml DNase I (Roche) in DPBS w/calcium and magnesium, for 1h under agitation in a water bath at 37°C. Digested tissue was separated at 700 x g for 10 min at 4°C, resuspended in SupHBSS and sequentially filtered through 100 µm, 70 µm and 40 µm nylon cell strainers previously hydrated with SupHBSS. After each filtration step, the cell suspension was separated and resuspended. Red blood cells were lysed with RBC buffer (ChemCruz) between the 70 µm and 40 µm filtration steps by incubating the cell pellet in 1

ml of 1X RBC for 2.5 min on ice, and inactivated with SupHBSS. The final cell suspension was separated and resuspended in magnetic beads buffer (MBB) consisting of DPBS w/o calcium and magnesium supplemented with 0.5% BSA and 2 mM EDTA, and filtered through 30 µm cell strainer. Cell sorting was carried out by incubating the cell pellet with anti-CD45 and anti-CD31 antibody to eliminate immune/hematopoietic and endothelial cells. Incubation with anti-7-integrin antibody yielded the satellite cell fraction. To precipitate contaminating fibroblasts, the 7-integrin positive fraction was pre-plated for 2h in growth medium consisting of DMEM high-glucose Glutamax (Gibco), supplemented with 1 mM sodium pyruvate, 1% pen/strep, 20% FBS, 10% horse serum, and 2% chicken embryo extract. Unattached cells were recovered and plated for proliferation in CytoGROW medium (Resnova) at a density of 200000 cells/100 mm dish. After 4 days of proliferation, cells were trypsinized and counted for analysis using a Seahorse XFe96 Extracellular Flux Analyser (Seahorse Bioscience-Agilent, USA). Bioenergetic profiles of skeletal muscle satellite cells isolated from $SOD1^{G93A}$ mice and wild-type age-matched controls were performed using a Mito Stress Test Kit (Seahorse Bioscience), following the manufacturer's instructions and according to Salvatori and collaborators (Salvatori et al., 2018).

Human samples and ethics statement

Muscle biopsies from ALS patients were obtained for diagnostic purposes in the Department of Medical, Surgical and Neurological Sciences of the University of Siena, Siena, Italy. All patients signed informed consent to permit the use of their samples for research. Our study complies with the ethical standards established in the 1964 Declaration of Helsinki and its later amendments.

Electrophoresis and western blotting

Protein samples were separated by SDS–polyacrylamide gel electrophoresis and transferred to nitrocellulose membranes (Perkin Elmer, Cat# NBA085B). Membranes were blocked for 1 h in Tris-buffered saline solution with 0.1% Tween-20 (TBS-T) containing 5% BSA, and then incubated for 2 h at room temperature or overnight at 4°C with indicated primary antibodies, diluted in TBS-T containing 2% BSA. After rinsing with TBS-T solution, membranes were incubated for 1 h with the appropriate peroxidase-conjugated secondary antibody diluted in TBS-T containing 1% BSA, then washed and developed using the enhanced chemiluminescence detection system (Roche Molecular Diagnostics, CA, USA, Cat# n11500694001 or BIO-RAD Clarity™ Western ECL substrate Cat# 170-5061). Densitometric analyses were performed using ImageJ (U. S. National Institutes of Health, Bethesda, Maryland, USA, https://imagej.nih.gov/ij/, 1997-2016). Protein relative expression values were normalized to GAPDH or β-Actin. The apparent molecular weight of proteins was determined by calibrating the blots with pre-stained molecular weight markers (Bio-Rad Laboratories, Cat# 161-0394).

DNA-RNA isolation and Real Time qPCR

Mitochondrial and genomic DNA were isolated according to Miller (Miller, 2003), whereas total RNA was extracted with Trizol and retro-transcribed with a SensiFASTtm cDNA synthesis kit (Bioline Cat# BIO-65054). Mitochondrial DNA content and mRNA expression levels were determined by Real Time qPCR reactions using a Light Cycler 480 SYBR Green System (Roche ETC). Cp values were calculated using the 'second derivative max' algorithm of the Lightcycler software. Relative mitochondrial DNA content was normalized to the genomic genes TNF-alfa and Interleukin 2 (IL2), whereas mRNA relative expression values were normalized to the housekeeping gene TATA box binding protein. Results, where not specifically expressed, were reported as the ratio between the average of

values from wild-type control mice and SOD1^{G93A} mice, normalized to the average values of genomic genes or the housekeeping gene. Primers sequences are listed in Table 3.

Treatment and assessment of motor function

In order to evaluate the best effective dose of drug, 110 day old SOD1^{G93A} transgenic mice and their wild-type control littermates (n=6 for each dose) were treated for seven days with or without Ranolazine (Selleckchem, catalog #S1425) (0 mg/kg, 25 mg/kg, 50 mg/kg, 100 mg/kg) by daily intraperitoneal injection. Motor ability were monitored as described in Ferraro et al., and in detail elaborated here, using the hanging grid test at days 0, 2, 5 and 7 of treatment; the average value from three trials (recorded from each mouse) was averaged to determine the final test score (Ferraro et al., 2016). Improvements in performance was expressed as a percentage of the starting value obtained at day 0, which was designated as 100%. After seven days of treatment, animals were euthanized by cervical dislocation and the TA and GNM muscles were rapidly excised for subsequent analyses.

The selected dose of Ranolazine (50 mg/kg) was then administered to SOD1^{G93A} transgenic mice at the onset of the disease (90 days old) and wild-type age-matched control mice. A control group of SOD1^{G93A} transgenic and wild-type age-matched control mice were treated with physiological solution. Mice were weighed and assessed by the hanging grid test once per week starting at beginning of treatment. The final weekly hanging grid score per mouse per week was determined as above. Groups of 120 day (n=12) and 150 day old mice (n=11/12) were sacrificed for evaluation of mid- and long-term treatment effects respectively. Survival was determined by noting the day at which animals achieved full paralysis of hind limbs and were not able to right within 30 s after being turned on the back. At this stage animals were sacrificed according to guidelines for preclinical testing (Poppe et al., 2014). In order to minimize sex related differences, we used male mice for both pilot and long-term treatments.

HPLC analysis of plasma ranolazine concentration

Plasma (100 ul) obtained from treated and untreated mice was added to 200 ul of acetonitrile, vortexed, and kept on ice for 5 min. The samples were then centrifuged for 10 min at 19000 RCF at room temperature, and the supernatants were subsequently diluted in solvent A (0,3% H_3PO_4) at a 1:1 (v:v) ration. 20 ul of each sample was injected into a HPLC system (series 200, Perkin Elmer) equipped with a Supelcosil LC-318 column (5um particle size, 25 cmx4.6mm). The isocratic HPLC elution mobile phase was composed of solvent A and solvent B (35% acetonitrile, 0,3% H_3PO_4) 10:90 (v:v). The flow rate was 0.8 ml/min and the column was maintained at room temperature. Total run time was 31 min and the retention time of ranolazine was 15.75 min. The UV/Vis detector was set at a wavelength of 223 nm.

Data analysis

Data are presented as mean ± SEM. Data were analysed using Kaplan-Meier, Student's t-test (two group comparison), one-way or two-way ANOVA. Post-hoc analysis was carried out using Bonferroni or Tukey tests. Statistical analysis was carried out using Graphpad Prism 5 software.

REFERENCES

Apolloni, S., Caputi, F., Pignataro, A., Amadio, S., Fabbrizio, P., Ammassari-Teule, M., and Volonté, C. (2019). Histamine Is an Inducer of the Heat Shock Response in SOD1-G93A Models of ALS. Int. J. Mol. Sci. 20.

Ferraro, E., Pin, F., Gorini, S., Pontecorvo, L., Ferri, A., Mollace, V., Costelli, P., and Rosano, G. (2016). Improvement of skeletal muscle performance in ageing by the metabolic modulator Trimetazidine. J. Cachexia. Sarcopenia Muscle 7, 449–457.
Ferri, A., Cozzolino, M., Crosio, C., Nencini, M., Casciati, A., Gralla, E.B., Rotilio, G., Valentine, J.S., and Carri, M.T. (2006). Familial ALS-superoxide dismutases associate with mitochondria and shift their redox potentials. Proc. Natl. Acad. Sci. U. S. A. 103, 13860–13865.
Giacovazzo, G., Apolloni, S., and Coccurello, R. (2018). Loss of P2X7 receptor function dampens whole body energy expenditure and fatty acid oxidation. Purinergic Signal. 14, 299–305.
Madaro, L., Marrocco, V., Carnio, S., Sandri, M., and Bouché, M. (2013). Intracellular signaling in ER stress-induced autophagy in skeletal muscle cells. FASEB J. 27, 1990–2000.
Miller, F.J. (2003). Precise determination of mitochondrial DNA copy number in human skeletal and cardiac muscle by a PCR-based assay: lack of change of copy number with age. Nucleic Acids Res. 31, 61e – 61.
Molinari, F., Pin, F., Gorini, S., Chiandotto, S., Pontecorvo, L., Penna, F., Rizzuto, E., Pisu, S., Musarò, A., Costelli, P., et al. (2017). The mitochondrial metabolic reprogramming agent trimetazidine as an 'exercise mimetic' in cachectic C26-bearing mice. J. Cachexia. Sarcopenia Muscle 8, 954–973.
Poppe, L., Rué, L., Robberecht, W., and Van Den Bosch, L. (2014). Translating biological findings into new treatment strategies for amyotrophic lateral sclerosis (ALS). Exp. Neurol. 262, 138–151.
Reggio, A., Rosina, M., Krahmer, N., Palma, A., Petrilli, L.L., Maiolatesi, G., Massacci, G., Salvatori, I., Valle, C., Testa, S., et al. (2020). Metabolic reprogramming of fibro/adipogenic progenitors facilitates muscle regeneration. Life Sci. Alliance 3.
Salvatori, I., Valle, C., Ferri, A., and Carrì, M.T. (2017). SIRT3 and mitochondrial metabolism in neurodegenerative diseases. Neurochem. Int. 109, 184–192.
Salvatori, I., Ferri, A., Scaricamazza, S., Giovannelli, I., Serrano, A., Rossi, S., D'Ambrosi, N., Cozzolino, M., Giulio, A. Di, Moreno, S., et al. (2018). Differential toxicity of TAR DNA-binding protein 43 isoforms depends on their submitochondrial localization in neuronal cells. J. Neurochem. 146, 585–597.

TABLE S1. Target genes and oligonucleotide sequences, Related to Figure 2, Figure 5, Figure 6, Figure 8, Figure S2, Figure S5.

Target	Forward sequence	Reverse sequence
TNF-alpha	5'-CTGTGAAGGGAATGGGTGTT-3'	3'-CCCAGCATCTTGTGTTTCTG-5'
IL2	5'TAGGCCACAGAATTGAAAGATCT-3'	3'-GTAGGTGGAAATTCTAGCATCATCC-5'
ND3	5'-CCCTTACGAGTGCGGCTTC-3'	3'-AGTGGCAGGTTAGTTGTTTGTAGG-5'
ND5	5'-AGCATTCGGAAGCATCTTTG-3'	3'-TCGGATGTCTTGTTCGTCTG-5'
COX3	5'-CACTAAATCAAGCCCTACTA-3'	3'-GAAATGGAGAATGATGTTTCA-5'
MyHCI	5'-TGCAGCAGTTCTTCAACCAC-3'	3'-TCGAGGCTTCTGGAAGTTGT-5'
MyHCIIa	5'-AGTCCCAGGTCAACAAGCTG-3'	3'-GCATGACCAAAGGTTTCACA-5'
MyHCIIx/d	5'-AGTCCCAGGTCAACAAGCTG-3'	3'-CACATTTGGCTCATCTCTTGG-5'
MyHCIIb	5'-AGTCCCAGGTCAACAAGCTG-3'	3'-TTTCTCCTGTCACCTCTCAACA-5'
Pgc1α	5'-GTCAACAGCAAAAGCCACAA-3'	3'-TCTGGGGTCAGAGGAAGAGA-5'
Glut-4	5'-GGCATGGGTTTCCAGTATGT-3'	3'-GCCCCTCAGTCATTCTCATG-5'
Nor1	5'-TACGCCACGCAGACTTATGG-3'	3'-TGGTCAGCTTGGTGTAGTCG-5'
Pdk4	5'-AAAGAGGCGGTCAGTAATCC-3'	3'-TCCTTCCACACCTTCACCACA-5'
Serca1	5'-CACCACCAACCAGATGTCAG-3'	3'-TCAAGACCTCTCCCTCAGGA-5'
Serca2a	5'-TCTCCTTGCCTGTGATCCTC-3'	3'-GCACCCGAACACCCTTATATT-5'
Serca2b	5'-AGTTGAGCCAGCAGACATTG-3'	3'-CCAGAGAATCATGCAAAAGACA-5'
Phospholamban (Pln)	5'-CACGTCAGAATCTCCAGAACC-3'	3'-GCTCTTCACAGAAGCATCACA-5'
Myoregulin (Mln)	5'-CAACGTTGCTAGGAGAACAC-3'	3'-GCTCTTGCCACTCATGTTCA-5'

Sarcolipin (Sln)	5’-TGAGGTCCTTGGTAGCCTGA-3’	3’-CACACCAAGGCTTGTCTTCA-5’
AchRα	5’-GGCTTTCACTCTCCGCTGAT-3’	3-’TCAGCGGCGTTATTGGACTC-5’
AchRε	5’-CTCTGCCAGAACCTGGGTG-3’	3’-GACAGTTCCTCTCCAGTGGC-5’
Nav1.5	5’-AGATGTCTCCCCCAGTAACCA-3’	3’-CTTGGGGAGCCTGTCTCTC-5’
Hdac4	5’-TGTACGACGCCAAAGATGAC-3’	3’-CGGTTCAGAAGCTGTTTTCC-5’
Myogenin	5’-TCAGACAGGGTCCATCCCAT-3’	3’-GCTGACTGTGAGCATCCACT-5’
MuRF-1	5’-GACAGTCGCATTTCAAAGCA-3’	3’-AACGACCTCCAGACATGGAC-5’
Myostatin	5’-CTGTAACCTTCCCAGGACCA-3’	3’-TCTTTTGGGTGCGATAATCC-5’
Myoglobin	5’-CTGTTTAAGACTCACCCTGAGAC-3’	5’-GGTGCAACCATGCTTCTTCA-3’
TATA box binding protein	5’-CCAATGACTCCTATGACCCCTA-3’	3’-CAGCCAAGATTCACGGTAGAT-5’